The 2015–2017 Pamir Earthquake Sequence: Fore-, Main-, and Aftershocks, Seismotectonics and Fault Interaction

Wasja Bloch[1*], Sabrina Metzger[1], Bernd Schurr[1], Xiaohui Yuan[1], Lothar Ratschbacher[2], Sanaa Reuter[2], Qiang Xu[3,4], Junmeng Zhao[3,4], Shokhruhk Murodkulov[5], Ilhomjon Oimuhammadzoda[6]

[1]GFZ German Research Centre for Geosciences, 14473 Potsdam, Germany
[2]Geologie, Technische Universität Bergakademie Freiberg, 09599 Freiberg, Germany
[3]Key Laboratory of Continental Collision and Plateau Uplift, Institute of Tibetan Plateau Research, Chinese Academy of Sciences, Beijing 100101, China
[4]CAS Center for Excellence in Tibetan Plateau Earth Sciences, Beijing 100101, China
[5]Institute of Geology, Earthquake Engineering and Seismology, National Academy of Sciences, Dushanbe, Tajikistan
[6]Department of Geology under the Government of the Republic of Tajikistan, Dushanbe, Tajikistan

Key Points:

- Pamir earthquake and moment tensor catalog (2015–2017), containing numerous fore- and aftershocks.
- Identification of the major seismotectonically active faults in the Pamir and southern Tian Shan
- Only a subordinate role of stress transfer in the triggering of large earthquakes, but indications for earthquake-activated fluid processes

*Now at: Department of Earth, Ocean and Atmospheric Sciences, University of British Columbia

Corresponding author: Wasja Bloch, `wbloch@eoas.ubc.ca`

Abstract

A sequence of three strong (M_W7.2–6.4) and several moderate (M_W4.4–5.7) earthquakes struck the Pamir Plateau and surrounding mountain ranges of Tajikistan, China, and Kyrgyzstan in 2015–2017. With a local seismic network in operation in the Xinjiang province since August 2015, an aftershock network on the Pamir Plateau of Tajikistan since February 2016, and additional permanent regional seismic stations, we were able to record the succession of the fore-, main-, and aftershock sequences at local distances with good azimuthal coverage. We located 11,784 seismic events and determined the moment tensor for 35 earthquakes. The seismicity delineates the major tectonic structures of the Pamir, i.e., the thrusts that absorb shortening along the plateau thrust front, and the strike-slip and normal faults that dissect the Plateau into a westward extruding and a northward advancing block. Fault ruptures were activated subsequently at increasing distances from the initial M_W7.2 Sarez. All mainshock areas but the initial one exhibited foreshock seismicity which was not modulated by the occurrence of the earlier earthquakes. Modelling of the static Coulomb stress changes indicates that aftershock triggering occurred over distances of $\leq$90 km on favourably oriented faults. The rupture of the second largest M_W6.6 Muji earthquake of the sequence happened despite its repeated stabilization through stress transfer in the order of -10 kPa. To explain the significant accumulation of M_W6+ earthquakes, we reason that the initial mainshock may have increased nearby fault permeability, and so facilitated fluid migration into the mature fault zones eventually triggering the later large earthquakes.

Plain Language Summary

A sequence of strong and moderate earthquakes occurred in the Pamir highlands and its surrounding mountain ranges between 2015 and 2017. We had a dense network of seismometers in operation, which recorded the earthquakes closely. We observed in total 11,784 smaller earthquakes that occurred before and after the largest ones. Of 35 earthquakes we could determine how their rupture plane was oriented. Our dataset traces the tectonic structures along which mountain building takes place. It shows how the Pamir Plateau is growing over the adjacent basins and is diagonally dissected in the middle. The later of the largest earthquakes occurred at subsequently greater distances from the first one and all but the first large earthquake were preceded by many smaller ones. The stress that the earlier earthquakes exert on the later ones is high only at rather small

distances. For farther-located earthquakes such stresses are small and even negative for the second largest earthquake of the sequence. The transferred stresses cannot explain why so many strong earthquakes occurred during the sequence. We find indications that fluids were freed by the first earthquake, which then migrated through the faults and may have triggered some of the later large earthquakes.

1 Introduction

The Pamir occupies the northwestern tip of the India-Asia collision zone, where several major mountain belts—the Tian Shan, Kunlun Shan, Karakorum, and Hindu Kush—and two large depressions—the Tarim and Afghan-Tajik basins—converge (Figure 1). The Pamir represents Asian lithosphere far north of the Indus-Yarlung suture zone that separates Indian from Asian crust. Nonetheless, it exhibits some of the highest strain rates for an intra-continental setting, both within the broad India-Asia collision zone and globally (Kreemer et al., 2014). Deformation involves shortening and dextral strike-slip shear along its northern margin and sinistral strike-slip faulting and extension in its interior, the Pamir Plateau (Schurr et al., 2014). Between December 2015 and November 2016, one moment magnitude M_W7 and two M_W6+ earthquakes hit the Pamir Plateau and its northern margin, activating a major fault network. The sequence started with the December 7, 2015 M_W7.2 Sarez sinistral strike-slip earthquake, which ruptured three segments of the Sarez-Karakul Fault System (SKFS) with a total length of ~80 km (Figure 1a; Sangha et al., 2017; Metzger et al., 2020; Elliott et al., 2020). About 6 months later, the June 26, 2016 M_W6.4 Sary-Tash earthquake ruptured a reverse fault, probably in the Tian Shan basement below the Main Pamir Thrust System (MPTS; He et al. (2018); see section 4.3.), ~90 km NNE of the northern end of the Sarez rupture. Another 5 months later, the November 25, 2016 M_W6.6 Muji earthquake broke two segments of the Muji Fault (Bie et al., 2018; T. Li et al., 2019; J. Li et al., 2019), ~30 km SW of the Sary-Tash earthquake (Figure 1a). Even for a region as seismically-active as the Pamir, this sequence was unusual: Long-term earthquake bulletins (e.g., the Global Earthquake Model ISC-GEM; Di Giacomo et al., 2018; ISC, 2021) report only 19 M_W6.4+ earthquakes in the Pamir between 1900 and 2015, including four large aftershocks that occurred within 20 km and one year after the mainshock. The probability that the three recent M_W6.4+ earthquakes occurred independent of each other, i.e., following a Poisson process, is 0.05%.

The mechanism of their probable interaction on kinematically dissimilar fault zones and over comparatively large distances is unclear.

To the first order, large earthquakes accommodate relative displacements between tectonic units. If the rate of tectonic loading is low and constant over time, it can be estimated by evaluating the slip history of a fault over geologic time scales. For example, (Mildon et al., 2019) respectively (Toda et al., 1998) calculated loading rates of $\leq$22 kPa/yr for faults in the central Apennines (Italy) and 0.3–4.0 kPa/yr before the 1995 M_W6.9 Kobe (Japan) earthquake. An earthquake represents a local displacement source that exerts additional elastic stress on its surroundings; this additional stress may by far exceed the accumulated tectonic stress. It has repeatedly been demonstrated that aftershock seismicity occurs in volumes where the transferred stresses are positive (Toda et al., 1998; Stein, 1999; Ryder et al., 2012; Toda & Stein, 2020). Sometimes the transferred stresses triggered other mainshocks (in cascades of foreshocks) only recognized in hindsight (Ellsworth & Bulut, 2018; Chen et al., 2020; Schurr et al., 2020). Additional stresses that may explain the delayed triggering of aftershocks may stem from viscous relaxation of the lower crust or upper mantle beneath a large earthquake (e.g. Freed & Lin, 2001). Finally, the detection of regional transients at higher rates than the secular deformation (Tape et al., 2018; Bedford et al., 2020) challenges the assumption of constant tectonic stressing and may represent an external earthquake triggering mechanisms that is difficult to account for.

Since August 2015, we had a temporary seismic network in operation in the Xinjiang province, China. It recorded the initial December 2015 Sarez earthquake (Figure 1a). In February 2016, we deployed a network on the Pamir Plateau of Tajikistan in the vicinity of the Sarez earthquake rupture. The combined networks recorded then both, the June 2016 Sary-Tash and the November 2016 Muji earthquake sequences with a very good azimuthal coverage. Additional moderate earthquakes with their own fore- and aftershock sequences augmented the seismotectonic record. The overall sequence of events allows us to closely investigate the location, orientation, and kinematics of the seismically active faults in the region. These provide insight in the partitioning of deformation in the Pamir and allow studying the mechanics of fault interaction. In addition, we derive displacement-rates from interferometric synthetic-aperture radar (InSAR) data to detect aseismic deformation transients. We examine the spatio-temporal seismic activation patterns to investigate earthquake interaction and nucleation. We also revisit the crustal seismicity record of the August 2008–July 2010 Tian-Shan–Pamir Geodynamic Program (TIPAGE) deployment (Schurr et al., 2014; Sippl et al., 2014) to identify longer term seismicity patterns.

2 Neotectonic Framework

In the Pamir, northward displacement at rates of 13–19 mm/yr is currently accommodated along its margins by crustal shortening along the MPTS in the north—in particular the Pamir Frontal Thrust (PFT)—, the sinistral Darvaz Fault Zone in the west and northwest, the dextral Karakorum Fault System in the southeast, and the Kongur Shan-Taxkorgan Normal Fault System in the Chinese eastern Pamir (Figure 1; e.g., Chevalier et al., 2015; Ischuk et al., 2013; Jade et al., 2004; Metzger et al., 2020; Schurr et al., 2014; Zubovich et al., 2010, 2016). The Karakorum Fault System probably links with the Sarez-Murghab Thrust System via the Aksu-Murghab Fault Zone on the Pamir Plateau (Robinson, 2009; Rutte et al., 2017). The dextral transpressive Kashgar-Yecheng Fault System (Cowgill, 2010) linked shortening in the western Kunlun Shan and along the MPTS; since ∼5 Ma (Sobel et al., 2011) and up to now (Zubovich et al., 2010), the Pamir and the Tarim basin have been moving north at about the same rate, rendering the transform component mostly inactive. The Muji Fault links ∼E-W extension along the Kongur Shan Normal Fault System to the MPTS (T. Li et al., 2019; Schurr et al., 2014; Sippl et al., 2014). The Kongur Shan Normal Fault System has accommodated ≥35 km of ∼E-W extension, mostly since ∼7 Ma (Robinson et al., 2004, 2007; Thiede et al., 2013); extension and dextral strike-slip along the Muji Fault are ongoing, as implied by seismicity and the divergence of the Global Navigation Satellite System (GNSS) velocity field between the Pamir's interior and Tarim block (T. Li et al., 2019; Zubovich et al., 2010).

In the Pamir interior the active displacement field is composed of bulk northward movement combined with ∼E-W extension (Zhou et al., 2016; Ischuk et al., 2013). The crust hosts both sinistral strike-slip faulting on ∼NE-striking or conjugate planes and—to a lesser degree—normal faulting on ∼N-striking planes (Schurr et al., 2014). In the eastern Pamir's interior the lack of both, thrusting and significant seismicity demonstrate that it is moving northward en bloc; this is in agreement with the GNSS data. The only ∼NE-striking sinistral-transtensive fault system of the Pamir interior, which has a clear morphologic expression and is seismically active, is the SKFS. It stretches from south of Lake Sarez to north of Lake Karakul (Elliott et al., 2020; Metzger et al., 2020; Schurr et al., 2014; Strecker et al., 1995). The northern SKFS is interpreted as a horst-graben structure (Nöth, 1932; Strecker et al., 1995), the southern SKFS currently shows dominant sinistral strike-slip and subordinate normal displacements (Elliott et al., 2020; Metzger et al., 2017). The ∼E-W extension—increasing into the western Pamir—is driven by westward gravitational collapse of thickened Pamir-Plateau crust into the Tajik Depression (Metzger et al., 2017; Schurr et al., 2014; Stübner et al., 2013).

Beneath the Pamir, Asian lithosphere forms a ∼90° arc that is retreating northward and westward as traced by intermediate-depth seismicity (60–300 km; Schneider et al., 2013; Sippl, Schurr, Tympel, et al., 2013). Kufner et al. (2016) and Bloch et al. (2021) inferred that the Asian slab retreat is forced by indentation of Indian lithosphere, bulldozing into the lithosphere of the Tajik-Tarim basin at mantle depth. In this context, the SKFS and the two largest earthquakes in the Pamir interior—the December 2015 and the 1911 M_W ∼7.3 (Kulikova et al., 2016) earthquakes—with similar sinistral strike-slip mechanisms in about the same region, likely express the underthrusting of the northwestern leading edge of an Indian mantle lithosphere indenter. The 2015 Sarez rupture may be the most recent manifestation of the shear zone at the northwestern tip of the indenter, building a continuous fault zone along the indenter's western edge and connecting the distributed sinistral fault zones of the Hindu Kush with the SKFS (Kufner et al., 2018, 2021; Metzger et al., 2017; Schurr et al., 2014).

3 Data and Methods

3.1 Seismic Data

We operated the East Pamir seismic network (FDSN code 8H; Yuan, Schurr, Bloch, et al., 2018) with 30 sites in the eastern Pamir, northwestern Kunlun, and northwestern Tarim Basin between August 2015 and July 2017, and the Sarez-Pamir aftershock seismic network (FDSN code 9H; Yuan, Schurr, Kufner, & Bloch, 2018) with 10 sites on the Pamir Plateau between February 2016 and July 2017 (Figure 1a). We used additional seismic waveform data from the Xinjiang regional seismic network (SEISDMC, 2021) and the Tajik National Seismic Network (FDSN code TJ; PMP International (Tajikistan), 2005).

We detected 39,309 seismic events using the *Lassie* earthquake detector as coherent peaks in move-out corrected, smoothed, pulse-like seismogram image functions that were stacked on a rectangular grid of 100×100×10 trial subsurface points with a spacing of 10×10×30 km (Comino et al., 2017) using the 1-D velocity model of Sippl, Schurr, Yuan, et al. (2013). The initial location and predicted P- and S-wave arrival times were used as a starting point for phase arrival time picking. We picked P-wave arrival times automatically with *MannekenPix* (Aldersons, 2004), where *obspy*'s STA/LTA triggers and predicted arrivals from the detection routine were used as starting points; S-wave arrival times were picked with *spicker* (Diehl et al., 2009). Filter window lengths and positions for both algorithms were calibrated with manually picked phase arrivals of 59 events. After each picking run, events were located with *hypo71* (Lee & Lahr, 1972), and arrival times with the highest residuals were removed until the location root-mean-square (RMS) misfit fell below a threshold of 2 s for P-waves and 3 s for P- and S-waves combined. We then used a subset of 1,855 seismic events with the best constrained arrival-time picks to invert for a 1-D velocity model and static station corrections using *velest* (Kissling et al., 1994). We removed arrival times that yielded a residual 5 times larger than the standard deviation of all residuals of a certain seismic phase on a certain station, resulting in preliminary locations for 29,795 events. We excluded apparent high-RMS misdetections (e.g., teleseismic events or network-wide null data in the XJ network), events with less than 6 arrival time picks, and events below 300 km depth. We manually revised the picks of 82 events of special interest, such as mainshocks or major foreshocks. After this step, we successfully located 11,782 seismic events in the 3-D P-wave velocity model of Bloch et al. (2021) with *simulps* (Thurber, 1983). The depth of 2,352 likely shallow events could not be resolved. They are located at the surface (i.e., the top boundary of the velocity model at -3 km). We computed waveform cross-correlation differential arrival times of event pairs less than 10 km apart with *obspy* (Krischer et al., 2015) and determined refined relative event locations for 3,748 events using differential P- and S-wave catalog- and cross–correlation-arrival–times in *hypoDD* (Waldhauser & Ellsworth, 2000).

3.2 Regional Moment Tensors

We determined regional moment tensors using the *RMT* algorithm of Nábělek and Xia (1995). Local Green's functions were computed with the discrete wavenumber summation method of Bouchon (1981) from the velocity and damping structure previously obtained by Sippl, Schurr, Yuan, et al. (2013). Seismograms were band-pass filtered between periods of 15 and 40 s for smaller events and 20 and 80 s for larger events, and restituted to true ground displacement. Noisy waveforms were discarded interactively. We allowed small timing adjustments between observed and synthetic seismograms to match the phase. In total, we were able to retrieve 35 moment tensors of events with moment magnitude M_W between 3.7 and 5.7. Moment tensors of the three large mainshocks could not be computed due to clipped waveforms; we instead report the moment tensor and magnitude published by the National Earthquake Information Center (NEIC).

A comparison between moment tensors and magnitudes of 9 events that were also analyzed by NEIC shows that the focal mechanisms agree (Figure S1). Significant differences occur only for two events from the Sary-Tash aftershock sequence (#9 and #12 in Figure S1a). Within the context of our other mechanisms in the sequence, and given our better database, we are confident in our solutions. NEIC moment magnitudes are consistently offset by M_W+0.3 (Figure S1b). We verified our response functions and processing routine and suspect that the shift stems from the different Earth models used.

3.3 Magnitudes

Calibrated local magnitudes M_L were obtained for all events by investigating the largest horizontal ground displacement amplitude A as a function of distance R. Following Bormann and Dewey (2012), we corrected the seismograms from their respective instrument response function and convolved them with the one of a Wood-Anderson seismograph. We measured the largest amplitude of any of the horizontal components. We calibrated the magnitude–amplitude–distance-relationship (Bormann & Dewey, 2012):

$$M_L^i = \log_{10} A^i + B \log_{10} R^i + C R^i + D \tag{1}$$

by minimizing:

$$\epsilon = \frac{1}{N} \sum_{i=1}^{N} \sqrt{\left(M_L^i - M_W^i\right)^2} \tag{2}$$

for all 958 station observations i of the 35 events for which M_W was available (Figure S1c). We report the so calibrated M_L as the mean value of M_L^i after removal of outliers.

3.4 Regional Unit Stress Tensor

We computed double-couple focal mechanisms from the 35 moment tensors (excluding the three largest mainshocks) and inverted them for the deviatoric regional unit stress tensor $\hat{S}$ using the *slick* toolbox (Michael, 1984, 1987). We minimized the misorientation between the slip vector and the predicted largest shear stress on the fault plane. We resolved the nodal plane ambiguity of most focal mechanisms by choosing the fault planes based on nearby mapped faults and aftershock lineations where possible; for the rest, we searched all stress tensors in angle intervals of 2° and shape factor intervals of 0.1 for the one that resulted in the lowest combined misorientation and selected the respective nodal plane with the lower misorientation as fault plane (Gephart & Forsyth, 1984). We then inverted the slip directions on these fault planes for $\hat{S}$.

3.5 InSAR Displacement and Fault Creep Model

To investigate possible creep on the SKFS, we analyzed automatically generated radar interferograms from the Comet LiCS data server (Lazecky et al., 2020) of ascending frame 100A_052 and descending frame 005D_050 (following Comet LiCS naming convention), covering the southern and northern part of the SKFS, respectively. We included all available data following the Sarez mainshock, that is 27 months for the southern frame (36 radar scenes, 93 interferograms; Figure S2), and 5 months for the northern frame (5 radar scenes, 7 interferograms, Figure S3), which were affected by the Sary-Tash earthquake thereafter. We therefore excluded subsequent acquisitions. After a visual data inspection and manual unwrapping error correction we calculated linear displacement rates using the small-baseline time-series analysis software *LiCSBAS* (Morishita et al., 2020). We subsampled (multi-looked) the original interferograms four times to a spatial resolution of ∼400 m, clipped them to the area of interest and subtracted the predicted atmospheric signal delay using state-of-the-art weather models (Yu et al., 2018). We applied a temporal low-pass filter of 42 days and a spatial low-pass filter of 2 km to the time-series of frame 100A_052, and no filter to frame 005D_050 (Hooper, 2008). Then we extracted linear rate maps (Figure S5).

We converted the rate maps into displacement accumulated over the 202 days between the Sarez and Sary-Tash mainshocks, assuming a constant displacement rate due to post-seismic slip within the first few months following the Sarez main shock. We modeled the observed surface displacements using vertical, rectangular dislocation sources (Okada, 1985) with uniform sinistral slip. Source location, depth and amount of slip were modified interactively using *kite* (Isken et al., 2017) until the predicted surface displacements fitted our observations reasonably well.

3.6 Coulomb Stress Changes

We modeled whether the stresses induced by the large earthquakes and corresponding foreshocks load or unload nearby fault segments by computing the change in Coulomb failure stress ΔCFS (Harris, 1998):

$$\Delta CFS = \Delta\tau + \mu(\Delta\sigma_n + \Delta p). \tag{3}$$

$\Delta\tau$ is the change in shear stress on the fault (positive in slip direction), $\Delta\sigma_n$ is the change in normal stress (positive unclamping), Δp is the change in pore pressure inside the fault and μ is the rock friction coefficient. Positive stresses point outward; a positive ΔCFS acts destabilizing. For most rocks μ is between 0.6 and 0.8 (Harris, 1998). Under the assumption of undrained conditions (the pore fluids do not escape or enter the fault), Δp is proportional to the mean stress change inside the fault (Rice & Cleary, 1976):

$$\Delta p = -\beta\frac{\Delta\sigma_{kk}}{3}, \tag{4}$$

where $\Delta\sigma_{kk}$ is the sum of the diagonal elements of the stress tensor and β is the Skempton coefficient. β lies between 0.5 and 1.0 for rocks, but is typically between 0.7 and 0.9 (Harris, 1998; Cocco & Rice, 2002). β and μ are often combined into the apparent friction coefficient:

$$\mu' = \mu(1-\beta). \tag{5}$$

We modeled stress changes in response to the largest earthquakes, foreshocks and post-seismic slip transients using *pscmp* (Wang et al., 2006). We constructed dislocation sources (Okada, 1985) from published fault-slip models (Metzger et al., 2017; He et al., 2018; Bie et al., 2018) and our own earthquake moment tensors. Fault dimensions for moment tensor sources were estimated from M_W using the scaling relationships of Wells and Coppersmith (1994); fault slip s was calculated from $M_0 = AGs$, with the seismic moment M_0, fault area A, and shear modulus $G = 32\,\text{GPa}$. We then computed the Coulomb failure stress changes according to Equations (3) and (4) at the origin times and on the fault planes of the three large earthquakes and significant foreshocks. We assumed Lamé's parameters $\lambda = 32\,\text{GPa}$ and $G = 32\,\text{GPa}$ and chose $\mu = 0.8$ and $\beta = 0.75$ so that the hypocenter of an earthquake has a positive ΔCFS, while remaining in the physically plausible range. We tested $\mu = 0.4$ and $\beta = 0.5$ as well as the debated assumption that $\Delta p = 0$ (Harris, 1998) by letting $\beta = 0$ and $\mu = \mu' = 0.2$. We found uncertainties in ΔCFS by varying μ, β, λ, and G with a standard deviation of 0.2, 0.2, 5 GPa, and 5 GPa, respectively, ensuring that β and μ remained in the [0, 1] range. We report the median, and the 5% and 95% quantiles of the resulting distributions.

4 Spatio-temporal Evolution of Seismicity

Seismicity in the studied time period was high and modulated by the occurrence of the three major earthquakes, which mark peaks in the detected earthquake rate (Figure 2). The Sarez mainshock ($A*$ in Figure 2a, * denotes the mainshock, specifically its origin) and early aftershocks occurred when only the 8H seismic network was in operation. Hence, the aftershock detection rate was relatively low (65 events/day at the maximum; Figure 2b). The later installation of the 9H network on the Pamir Plateau increased the sensitivity of the entire network significantly; this is obvious from the much higher maximum detection rates for the two following earthquake sequences ($\sim$180 events/day, $C*$ and $E*$ in Figure 2b). Other peaks in the event rate are due to the largest aftershock of the Sarez earthquake ($B*$), an earthquake swarm in the western Pamir (D), and M_W 4–5 earthquakes near Yarkant ($F*$), Khorog ($G*$), Karamyk ($H*$), and Taxkorgan ($I*$; Figures 2a and 2c; Table 1). We defined rectangular regions around the activated mainshock fault zones (A, C, E) and 15 km radii around the more moderate mainshocks (B, D, F–I) down to 50 km depth as the vicinity of each of the events (Figure 2a). Foreshocks are events that occurred in the so-defined vicinity and before the respective event with the largest magnitude, which is the respective mainshock.

The mainshocks $B*$–$I*$, following the Sarez earthquake, sequentially activated fault zones at increasing distance from $A*$ (Figure 2d). This sequential activity is not observed in the foreshock activity (Figure 2c and 2d); The vicinities A, B, C, D, E, and G were seismically active before the respective mainshocks—even years before, as recorded by the local TIPAGE seismic network (Schurr et al., 2014); this makes the distinction between foreshocks and background seismic activity only possible in retrospect. It is also not evident that the foreshock activity was triggered, enhanced or diminished by any mainshock. Phases of locally increased seismicity rate in the foreshock (Figure 2c) as well as aftershock series (Figure S4) represent subordinate aftershock sequences and do not correlate regionally. Only the vicinity B of the largest Sarez aftershock $B*$, which occurred $\sim$25 km from the Sarez epicenter, started to become seismically active immediately after $A*$.

Crustal seismicity that is not associated with any of the mainshocks delineates known neotectonic structures (Figures 1 and 2a): the MPTS exhibited diffuse seismic activity; the Kongur Shan Normal Fault System was seismically active between the Muji Fault and the northern end of the Taxkorgan Fault; and a swath along the Aksu-Murghab Fault Zone in the south-central Pamir was seismically active. In the following, we investigate the mainshock areas in detail.

4.1 Sarez Earthquake

The 2015 M_W7.2 Sarez earthquake ($A*$ in Figures 2, 3, and 4; Table 1) ruptured an ∼80 km long part of the SKFS between Lake Sarez and the Kokujbel Valley south of Lake Karakul (Elliott et al., 2020; Metzger et al., 2017; Sangha et al., 2017). Metzger et al. (2017) divided the rupture plane determined from InSAR data into three segments expressed as strike changes (Figure 3a). Of the southern segment the northern part was already seismically active during the August 2008 to July 2010 TIPAGE deployment (Figure 3b), but only one M_L2 event was detected near the fault plane in the 4 months between August 2015 and the Sarez mainshock (Figure 3b, ∼20 km from the hypocenter); no significant foreshock activity occurred before the Sarez earthquake.

The aftershocks of the Sarez earthquake skirted around the main co-seismic slip patch, with a concentration at the northern end of the rupture (Figure 3c; ∼60 km from the hypocenter) and sinistral transtensional focal mechanisms (Figure 3a). Aftershocks also concentrated ∼20 km south of the end of the co-seismically active fault patch (Figure 3c; -30 km), where the largest M_W5.1 aftershock $B*$ with a sinistral strike-slip mechanisms similar to the Sarez mainshock occurred 102 days later, and spawned its own aftershock series (Figures 2 and 3d).

The associated moment tensors exhibit both sinistral strike-slip and normal faulting. Neither the co- nor the post-seismic activity reactivated the ∼E-striking, Cenozoic thrusts and normal faults of this part of the Pamir (Figure 3a). The ∼NNE-strike of the normal-fault nodal planes are parallel to the many tensional surface-breaks mapped on ground along the northern segment (Figure 6 of Metzger et al., 2017) and the Quaternary-filled grabens, outlined on the 1:200,000 geological maps and traceable from topography (Figure 3a; Yushin et al., 1964). An important event of the earthquake sequence is the April 9, 2016 M_W4.1 dextral strike-slip event *c'* that occurred 124 days after the Sarez earthquake, ∼85 km north of the tip of its rupture plane, and 78 days before and ∼10 km east of the hypocenter of the Sary-Tash earthquake (Figures 2c, 3d, 4, 5).

4.2 Creep on the Sarez-Karakul Fault System

The accumulated InSAR line-of-sight (LOS) displacement between the Sarez and the Sary-Tash mainshocks shows a distinct change along the mapped SKFS (Figure 4a). While the data base of the southern frame is large enough to provide a good signal-to-noise ratio to detect tectonic signals in the time-series, the resulting rates in the northern frame—based on 5 radar scenes—may be dominated by local atmospheric conditions (Figure S5).

The southern frame probably highlights relative sinistral motion and potential uplift east of the SKFS of ∼8 mm in the look direction between the first satellite pass on December 30, 2015 and the Sary-Tash earthquake (Figure 4a). The sinistral sense of motion agrees with the co-seismic slip model of Metzger et al. (2017) and the displacement amplitude is reasonable as well (∼1% of co-seismic slip; Metzger et al., 2017), given that our observations do not capture the first three weeks of the afterslip history.

In the northern frame, earthquake focal mechanisms indicate sinistral slip along the SKFS-segments north of Lake Karakul (Figure 3a; see also Schurr et al., 2014). Even though the view direction is nearly insensitive to lateral slip, we assume—due to the significant across-strike displacement changes, the along-strike correlation of the signal, the seismic activity along the fault segments, and the location of events *c'* and C^* close to the northern tip of the SKFS—that the displacement signal is due to aseismic creep on the SKFS; this allows to test whether creep may have contributed to the triggering of the Sary-Tash earthquake. The positive sign west of the SKFS (the ground moved towards the satellite) indicates that the signal is not due to a normal faulting component.

We modeled our displacement observations as aseismic creep on seven vertical fault patches between 0.5 km and 10.5 km depth along two segments of the SKFS between the epicenters of the Sarez and the Sary-Tash earthquakes (Kokujbel segment in the south, Karakul segment in the north; Figures 3d and 4b). Our model indicates a maximum cumulative creep between 20 and 30 mm in the 202 days between the earthquakes on the Kokujbel segment (∼35–55 mm/yr, Figure S5), which occupies part of the slip patch of the Sarez earthquake. On the Karakul segment, we find a total maximum creep of 40 mm

(∼72 mm/yr) in the south to 25 mm (∼45 mm/yr, Figure S5) in the north. The segment links the co-seismically active part of the SKFS with the Kyzilart Transfer Zone, which connects the Muji Fault with the PFT (Figures 3a and 4a; Sippl et al., 2014)

4.3 Sary-Tash Earthquake

The Sary-Tash earthquake (C^* in Figures 2, 4, 5; Table 1) occurred in the MPTS, westerly adjacent to the 2008 M_W6.6 Nura earthquake (Schurr et al., 2014; Sippl et al., 2014; Teshebaeva et al., 2014; Qiao et al., 2015). The region—geologically poorly-mapped in the high-altitude terrain of the Tajik-Kyrgyz-China border triangle—is characterized by a complex network of faults with both ∼N- and ∼S-dips, making the choice of the fault plane from the two nodal planes non-trivial. NEIC reports a comparatively low double-couple component for the mainshock moment tensor of 86%, hinting at the complexity of the rupture process.

The vicinity of the earthquake partially overlaps with the intense aftershock volume of the 2008 Nura earthquake (Sippl et al., 2014) and was seismically active throughout the deployment periods of the different seismic networks covering the region; 13 small earthquakes (M_L1.6–3.7) were detected in the vicinity of the future Sary-Tash earthquake in the two months preceding the 2008 Nura earthquake during the TIPAGE deployment and 188 (M_L1.3–M_W4.3) in the 11 months before the Sary-Tash earthquake since the 8H network was active (Figures 5c and d). Foreshock activity was comparatively high compared to the Sarez and Muji mainshocks and peaked in 3 ∼1-month-long swarms in March, April and June 2016 (Figure 2c). Notably, the foreshocks after the April 9, 2016 *c'* event concentrated around the future hypocenter C^* in along-strike view (Figure 5c). The aftershocks of the Sary-Tash earthquake form an about vertical, ∼E-W-striking structure to ∼20 km depth east of the hypocenter (Figures 5b and 5e). Moment tensors display a variety of focal mechanisms, again testifying to a complex fault-zone geometry a depth (Figure 5a).

Fault-slip models of InSAR displacement maps slightly favor the steeply N-dipping nodal plane (FP1) over the gently ∼S-dipping one (FP2) for the Sary-Tash mainshock (He et al., 2018). If FP2 was the main fault plane, the aftershocks would crosscut it and be concentrated inside the volume of the largest slip (Figure 5b). This is contrary to what is observed for the Sarez (Section 4.1) and Muji (Section 4.4) earthquakes, and many other earthquakes worldwide, where aftershocks concentrate around the segments of highest slip (Das & Henry, 2003). We prefer the ∼N-dipping FP1 as the main fault plane, because with this choice, the aftershocks are located in the hanging wall and up-dip of the largest co-seismic slip (Figure 5b), a pattern that has also been observed for the 2008 Nura earthquake (Sippl et al., 2014). The hypocenter is located at the western end of the geodetically-determined co-seismic slip patch (He et al., 2018), at 11.9 km depth, to the west and at 8.6 km hypocentral distance of the M_W4.1 foreshock *c'* (Figure 5e). The variable aftershock focal mechanisms tend to have dextral-transpressive mechanisms on ∼E-striking planes, except for two normal faulting events at the eastern end of the rupture (Figure 5a). The ∼E-striking nodal planes of the strike-slip solutions are interpreted to carry the dextral strike-slip deformation identified in the background seismicity of the TIPAGE deployment data and by geological fault-slip analysis within the MPTS and in the Kyzilart Transfer Zone; even the normal-fault earthquakes, indicating E–W extension, have neotectonic fault equivalents, and were interpreted as interaction of the SKFS with the MPTS (Sippl et al., 2014). The hypocenter depth and N-dip of the Sary-Tash earthquake fault suggest that the earthquake re-activated a basement fault in the footwall of the PFT, as such faults are common in the Tian Shan immediately to the north (Figure 1b). In contrast, the 2008 Nura earthquake ruptured a ∼S-dipping plane; its hypocenter lay at 3.4 km depth and thus likely in the MPTS imbricate stack. That the Sary-Tash and Nura aftershock activities hardly overlap along strike, occupy different depth intervals, and differently-dipping patches again indicate that they activated different faults (Figure 5). Another difference is that the shallow Nura earthquake re-activated several pre-existing NE- and NW-striking faults in the Tian Shan during its regionally-extensive aftershock sequence; the deeper Sary-Tash earthquake did not. The M_W4.8 foreshock to the Muji earthquake *e'*, and its mainshock hypocenter E^* occurred 153 days later on the Muji Fault, ∼35 km southeast of the end of the rupture plane of the Sary-Tash earthquake. This configuration likely connects the MPTS in the area of the Sary-Tash earthquake with the Muji Fault along the Kyzilart Transfer Zone.

4.4 Muji Earthquake

The rupture plane of the 2016 M_W6.6 Muji earthquake (E^* in Figures 2 and 6; Table 1) broke near simultaneously in two main slip patches; a third slip patch modeled below ∼20 km depth is unresolved (Bie et al., 2018). The area of the eastern slip patch was seismically active during the TIPAGE and the current deployment (2015–2017; Figure 6b). The M_W4.8 Muji foreshock *e'* occurred only 12 minutes before the mainshock, at the western end of the rupture plane and ∼460 m hypocentral distance. We identified a series of four more foreshocks between the *e'* and E^* in the seismogram of the closest station EP10 but could not locate them. The mainshock hypocenter was at 13.7 km depth. Aftershocks concentrated around and below the highest slip zone at the WNW' end of the rupture plane, tightly constrained to the rim of the main slip patch; they continued ∼10 km beyond its ESE' end of the eastern slip patch.

Fore- and aftershock moment tensors exhibit right-lateral focal mechanisms similar to the mainshock. Notably, the two western focal mechanisms have a small reverse faulting component, while the two eastern ones have a small normal faulting component, a fault kinematic that was also observed in the morphology of the surface breaks (T. Li et al., 2019). This is compatible with the transition from the nearly purely extensional faulting along the Kongur Shan Normal Fault System to the dextral-transpressional Kyzilart Transfer Zone and MPTS.

4.5 Northwest Pamir Earthquake Swarm

An earthquake swarm of 80 events occurred on the western side of Pamir's Academy of Sciences Range, hosting Pamir's highest peaks (*D* in Figures 2 and 7; Table 1). It was active throughout the deployment of the Sarez aftershock network (Figure 2c), with an activity peak, including the largest M_W4.4 event D^*, in August 2016. Focal mechanisms indicate normal faulting on ∼N(NW)-striking planes. Well-located hypocenters and moment tensor centroids show that most seismicity clustered at shallow depth (≤6 km; Figure 7). Such normal-faulting solutions are—together with strike-slip solutions—typical for the western Pamir, the part of the Pamir Plateau that shows westward-increasing collapse of crust into the Tajik Depression (Kufner et al., 2018; Schurr et al., 2014).

4.6 Yarkant Earthquake

On January 20, 2017 an M_W4.7 earthquake occurred 53 km southwest of Yarkant, Xinjiang (F^* in Figures 2 and 7; Table 1). Three events were detected in *F* before the earthquake—one of them only 55 minutes before the mainshock—and a total of 41 aftershocks. The moment tensor indicates thrusting on either a shallowly- or steeply-dipping fault plane. Seismicity aligns along a ∼N-striking structure (Figure 7), paralleling the topographic slope and the strike of a shallowly-dipping nodal plane. We interpret these earthquakes to record top-to-NE thrusting along ∼SW-dipping faults, compatible with the growth of the eastern Pamir into the Tarim Basin (Figures 1 and 7).

4.7 Khorog Earthquake

On March 22, 2017, a M_W4.6 earthquake occurred ∼51 km ENE of Khorog, Tajikistan (G* in Figures 2 and 7; Table 1). The vicinity of the earthquake was active throughout the deployment of the 9H network with 24 seismic events detected before the mainshock. Whether the structure was activated by the Sarez earthquake—whose hypocenter is located ∼90 km NE of the earthquake—is unclear, because of the limited sensitivity of the network before the 9H network deployment. Two ∼NE-trending streaks of seismic activity can be identified in map view; the focal mechanism indicates sinistral strike-slip on a ∼NE-striking fault. The depth of the earthquake is not well constrained due to the limited network coverage (Figure 7). The earthquake cluster lies along a fault zone classified as likely active by Stübner et al. (2013) and Schurr et al. (2014) due to linear topographic expressions; the fault zone coincides with the southeastern part of the Pathus-Nemos Fault of Strom (2014); it overprints the Miocene dextral-normal Gund shear/fault zone at an acute angle (Figures 1b; Worthington et al., 2020). Elliott et al. (2020) proposed this fault zone as the source of the 1911 Sarez earthquake. As a mappable continuation of the neotectonic fault network at the southern continuation of the SKFS (Figure 1b), we interpret the Khorog earthquake cluster as part of the distributed faults that connect the SKFS with the sinistral fault zones of the Hindu Kush (e.g., the Chaman, Panjshir, Central Badakhshan Fault Zones; Figure 1b), outlining a continuous fault zone along the western edge of the Indian indenter at mantle depth (Section 2; Metzger et al., 2017).

4.8 Karamyk Earthquake

An M_W5.8 earthquake happened on May 3, 2017 near the Kyrgyz-Tajik border, ∼25 km west of the settlement of Karamyk, Kyrgyzstan (H* in Figures 2 and 7; Table 1). The event was outside of the network, but due to the relatively large magnitude some aftershock seismicity could be located and the moment tensors of the mainshock and one aftershock be determined. The seismicity outlined a ∼NE-trending cluster, with a dextral strike-slip- and a reverse-faulting focal mechanism for the mainshock and an aftershock, respectively (Figure 7). The cluster lies along a Cenozoic fault zone in the Tian Shan, outlined by partly overthrusted Jurassic-Paleogene basin strata; geological fault-slip analysis along the eastern strands of these fault zone reveals top-to-NW thrusting with a dextral strike-slip component (stations TS19 to TS22 in Figure S7 in Kufner et al., 2018).

4.9 Taxkorgan Earthquake

The last moderate earthquake detected during our recording period was the $M_W 5.2$ Taxkorgan earthquake on May 10, 2017, ~23 km south of Taxkorgan, Xinjiang (I^* in Figures 2 and 7; Table 1). Aftershock seismicity and the focal mechanism indicate that it reactivated a steeply ~ENE-dipping segment of the Taxkorgan Normal Fault (Robinson et al., 2007). 14 foreshocks preceded the earthquake, half of them in the two months after the Muji earthquake (Figures 7 and 8). The Taxkorgan Normal Fault can be interpreted as part of the Kongur Shan–Taxkorgan Normal Fault System, with a southward decreasing amount of extension (Figure 1).

5 Regional Stress Field

Inversion of crustal fault-slip data from focal mechanisms yielded the regional deviatoric unit stress tensor (in north–east–down-convention):

$$\hat{S} = \begin{pmatrix} -0.835 & 0.627 & -0.042 \\ 0.627 & 0.969 & 0.084 \\ -0.042 & 0.084 & -0.134 \end{pmatrix}. \tag{6}$$

It indicates near-horizontal, N18°W-oriented compression, σ_1, and N73°E-oriented extension, σ_3, with a near-vertical, 85° S-plunging σ_2 axis (Figure 7). The stress field is dominantly strike-slip with a normal faulting component. σ_1 is about parallel to the GNSS vectors in the Pamir interior and σ_1 at mantle depth (Bloch et al., 2021). σ_2 has a compressional component, represented by the shape factor $\frac{\sigma_2-\sigma_1}{\sigma_3-\sigma_1} = 0.41$, or the compensated linear vector dipole component of the stress tensor of 23%. The vertical compression component is interpreted to reflect the bulk thinning of the crust of the Pamir Plateau due to its westward (in the σ_3-orientation) collapse into the Tajik Depression.

6 Coulomb Stress Changes

6.1 Main Pamir Thrust System and the Sary-Tash Earthquake

Our preferred model for ΔCFS induced by the Sarez earthquake onto the Sary-Tash earthquake is along a ~N-dipping fault in the footwall of the PFT (Figure 8). Figure S6 shows the contributions of the individual slip sources and the effect of variations in β and μ. We chose the fault parameters of He et al. (2018), as they predicted the highest and most localized Coulomb stress change on the hypocenter. The fault parameters derived from the moment tensors published by GEOFON and NEIC yielded smaller stress concentration at the hypocenter and on the fault plane.

The Sarez earthquake caused a long-wavelength positive ΔCFS on Sary-Tash earthquake fault with the highest values in the shallowest and westernmost part investigated. It loaded the rupture plane, foreshock *c'*, and hypocenter only weakly (~3 kPa; Figure S6). The predicted rake at the hypocenter is dextral with a normal faulting component, lacking the observed reverse faulting component. Creep on the SKFS (Figure 4) additionally loaded the Sary-Tash earthquake fault, mainly in the upper westernmost part, but with a lobe of increased ΔCFS that reaches towards the hypocenter at ~10 km depth. East of the hypocenter, the foreshock *c'* loaded the rim of the rupture plane. Together they caused a ΔCFS concentration of 5^{+3}_{-1} kPa at the hypocenter (Table 1 Figure S7). The predicted rake at the hypocenter retains a distinct normal faulting component (Figure 8b). Adding the regional stress (based on our stress inversion) with a magnitude of 30 kPa brings the hypocenter and the entire rupture plane into the observed reverse faulting domain. The sign of ΔCFS due to the regional stress depends on β and μ and is sensitive to the magnitude of σ_2, which is not well constrained in our inversion. Static stress change induced by the 2008 Nura earthquake was in the order of $\leq$1 MPa (Figure S6), loaded the fault, but did not immediately trigger the Sary-Tash earthquake.

We conclude that the sum of stresses exerted by the Sarez earthquake, foreshock *c'*, and post-seismic creep only reach a few kPa. Loading by the regional stress is required to explain the slip direction. Despite a strong stress perturbation by the 2008 Nura earthquake, the Sary-Tash earthquake did not rupture before 2016.

6.2 Muji Fault

The preferred ΔCFS model for the Muji earthquake is shown in Figure 9 with the contribution of the individual stress sources shown in Figure S8. We selected the fault parameters of Bie et al. (2018); the parameters derived from the moment tensors published by GEOFON and NEIC yielded identical results. The Sarez and Sary-Tash earthquakes unloaded the fault plane of the Muji earthquake with a negative ΔCFS of -19^{+7}_{-6} kPa (Figure S9, Table 1). For the Sarez earthquake, the effect is mostly due to clamping of the Muji fault through normal stress and a slight loading opposite to the slip direction, i.e., a relaxation in slip direction. The Sary-Tash earthquake imposed left-lateral strain on the Muji fault, as it pulled the northern wall more towards the northwest relative to the southern wall; the predicted left-lateral slip is in contrast to the observed right-lateral slip of the earthquake (Figure 9b). The 2008 Nura earthquakes imposed left-lateral slip on the Muji fault, unloading it similarly to the Sary-Tash earthquake.

The foreshock *e'* imposed a strong (∼90 kPa) positive ΔCFS on the hypocenter. However, the remainder of the fault plane remained in the unloaded and clamped state described above and—as the foreshock has a focal mechanism and location almost identical to the mainshock—our model can neither explain triggering of *e'* through CFS changes.

The principal axis orientations of the moment tensor of the Muji earthquake and foreshock *e'* align with those of our regional stress tensor (Figure 7), suggesting that they are close to optimal oriented in the regional stress field. An additional minimum regional stress magnitude ≥30 kPa is required to reverse the stabilizing static stress changes of the previous large earthquakes and to impose a positive ΔCFS of 5–15 kPa on the rupture plane (Figure 9c). The resulting ΔCFS pattern correlates with the distribution of aftershock seismicity, where the western continuation of the rupture plane (that had no aftershock seismicity) shows a negative δCFS, while its eastern continuation (where aftershocks extend beyond the end of the rupture) shows a positive ΔCFS (Figure 9c). We conclude that static stress changes counteracted the pending rupture and that slip occurred primarily due to secular loading by tectonic stresses.

6.3 Moderate Earthquakes

Among the other moderate main-, fore- and aftershocks of the sequence with an available moment tensor (Figure 7, Table 1), earthquake triggering through Coulomb stress transfer can be observed for events located at intermediate distance (5–50 km) from a previous mainshock (#s *4*, *5*, *6* (*B**), *8* (*c'*), *10*, *16*, *17*, *20–23*, *30*, *31* (*G**), *33*, *35*; Figure 7 and Table 1). These events typically show a positive ΔCFS between 10s and 100s kPa on their fault plane, even though the predicted rake deviates from the observed one by 10s of degrees.

The aftershocks that reside very close to or on the rupture plane of a previous earthquake (#s *2*, *3*, *7*, *9*, *11–15*, *18*, *19*, *25–27*) often show a negative ΔCFS (∼-10 kPa to -1 MPa). This apparent stabilization of aftershock hypocenters is an artifact of the fault-slip models that were created from smoothed differential surface displacement maps or from uniform rectangular dislocation sources. Both lack small scale slip heterogeneities that may rupture in aftershocks. Additionally, the InSAR fault-slip models fit interferometric phase differences observed between two images that were acquired within 24 days (Bie et al., 2018; He et al., 2018; Metzger et al., 2017). This time interval results in a mainshock slip model that implicitly includes the slip of the early aftershocks.

Earthquakes located at larger distances from the large earthquakes (#*28* (*F**), *32* (*H**), *34* (*I**)) received no more than a miniscule ΔCFS from the stress changes caused by the large mainshocks. However, as for Muji foreshock *e'*, occurrence of these earthquakes can be explained in the regional stress field. Usually a regional stress magnitude of 10s kPa are enough to rotate the predicted to the observed slip, yielding a positive CFS (Figure S4).

7 Discussion

7.1 Seismotectonics

Tectonically, the earthquake sequence recorded between August 2015 and July 2017 outlines the first-order deformation field of the Pamir and southernmost Tian Shan. The northward displacement of the eastern Pamir Plateau, tied to the Tarim-Basin lithosphere, is absorbed to a large extent along the Pamir front, the MPTS. Basement-rooted faults of the Paleozoic Tian Shan orogen, that have been re-activated since ∼12 Ma (e.g. Käßner et al., 2016; Abdulhameed et al., 2020), most recently yielded during the the Sary-Tash (*C**) and Karamyk (*H**) earthquakes on both ends of the Alai Valley, where the MPTS interacts with the Tian Shan. This requires the activation of a basal detachment deeper than that of the MPTS in Jurassic evaporites, that governs the fold-thrust belt of the

Tajik Depression (e.g. Bekker, 1996; Gagała et al., 2020). About E–W extension in the eastern Pamir along the Kongur Shan-Taxkorgan Normal Fault System (I^*), with northward increasing amounts (Robinson et al., 2007), is transferred into dextral strike-slip along the Muji Fault, and—under increasingly transpressional deformation—via the western Muji Fault and the Kyzilart Transfer Zone into and across the MPTS to the PFT; the latter is characterized by range-front segmentation in thrusts and dextral strike-slip faults (e.g. Arrowsmith & Strecker, 1999; Sippl et al., 2014).

The Pamir Plateau is dissected by the SKFS into the relative aseismic eastern Pamir block and the western Pamir with higher seismic activity (Schurr et al., 2014). Although we concur with the interpretation that the SKFS is part of the broad and distributed zone of sinistral strike-slip faulting along the western margin of the Indian mantle lithosphere indenter (Metzger et al., 2017), several aspects of this fault zone are particular: (1) The two largest historical crustal earthquakes of the Pamir interior—the 1911 and 2015 Sarez earthquakes—occurred at the southern end of the SKFS, approximately above the northeastern tip of the indenter (Figure 1b); (2) the SKFS is morphologically well-expressed along the Sarez, Kokujbel, and Karakul segments, but loses expression entering the MPTS and the southwestern Pamir; (3) neotectonically, the northern Kokujbel and Karakul segments show the clearest evidence of ~E-W extension, suggesting a northward increasing extensional component (from the Sarez to the Karakul segments), akin to that of the Kongur-Shan-Taxkorgan Normal Fault System. We speculate that the SKFS nucleated above the tip of the indenter and has been growing towards the NE and SW. The northward-increasing transtensional component in the Sarez aftershocks, the rift appearance of the Karakul segment, the anticlockwise change in strike of the northernmost SKFS segments, and the (little-studied) merger of the these strands with the MPTS (Figures 1b and 4) suggest increasingly stronger westward motion of material from the eastern Pamir in the east to the Tajik Depression to the west, and from the Hindu Kush and Karakorum in the south to the front of the Pamir in the north; this is traced by the GNSS velocity vectors (Figure 1b; Metzger et al., 2020) and the anticlockwise rotations recorded in the northern Tajik Depression by paleomagnetic data (Pozzi & Feinberg, 1991; Thomas et al., 1994). The SKFS at and south of Lake Sarez and the dextral Aksu-Murghab Fault Zone and its western prolongation, the Sarez-Murghab Thrust System, may outline—on first-order—the triangular shape of the tip of the mantle indenter by distributed deformation in the crust (Figure 1b).

While the eastern Pamir is growing outward into the Tarim basin by thrusting ($F*$), the entire western Pamir has a significant component of ∼E-W extension, reflecting its collapse into the Tajik Depression. The westward increasing extensional component is accommodated by an increase in the dextral strike-slip component along the western MPTS (e.g., the Vakhsh Thrust System; Metzger et al. (2020); Figure 1b), and the involvement of the southern Tian Shan in the Pamir deformation field by thrusting and dextral strike-slip faulting ($H*$; for the similar neotectonic evolution see Käßner et al., 2016).

7.2 Earthquake Triggering

We demonstrated at the outset that the probability of the three earthquakes occurring by chance in such close vicinity in space and time is very low. We tested if static CFS changes from the consecutive earthquake ruptures are able to explain rupture triggering of the neighboring faults. ΔCFS has a strong effect in the near field but diminishes rapidly at distances greater than about one rupture length. It is positive for the aftershocks that occurred in the extension of the Sarez rupture, if the stress-receiving aftershock fault plane was favorably oriented. Hence, ΔCFS is a viable trigger for the moderate earthquakes in the southern continuation of the SKFS and the aftershocks to the north spanning Lake Karakul (e.g., events $B*$, $G*$ in Figure 2a, and *30* in Figure 7).

Predicted ΔCFS for the Sary-Tash earthquake and its foreshock *c'* may be as low as 4 kPa, if possible creep of the SKFS is not considered. Even with creep and favorable (low-β) fault parameters, ΔCFS at the Sary-Tash hypocenter does not exceed 10 kPa (Figure S7; see also Fialko et al., 2021). These values may be just above the tidal shear stresses that the dip-slip fault experiences over the course of a day (∼5 kPa; Tanaka et al., 2002). An additional ΔCFS contribution may be caused by viscous relaxation of the lower crust in the months following the Sarez earthquake, which would constitute an additional, deeper slip source with the same sense of motion and therefore a comparable effect as the earthquake itself. The time constant inherent to viscous processes might account for the time lag of 7 months between events $A*$ and $C*$ to over 15 months between event $A*$ and $G*$ (Table 1). But modeling of afterslip of the Sarez earthquake suggested that no visco-elastic relaxation took place (Fialko et al., 2021). In case of the Muji foreshock *e'*, negative ΔCFS values even indicate stabilization at the hypocenter and suggest that it ruptured *despite of*, not due to, the static stress changes imposed by the previous earthquakes. We cannot exclude that the complexity of the Sary-Tash earthquake, indicated by the diverse aftershock mechanisms and the high compensated linear vector dipole component of the moment tensor, may have caused a more complex deformation pattern below the MPTS; but we consider it unlikely that it reversed the modeled stress relaxation. Undetected triggered dextral creep on the Kyzilart Transfer Zone—that connects the PFT with the Muji Fault—may have imposed a positive ΔCFS that loaded the foreshock hypocenter. The occurrence of aftershocks east of the Muji mainshock rupture plane but not west of it may suggest that the western continuation of the Muji Fault was not critically stressed; either because it has been relaxed by the sinistral far-field strain of the Sary-Tash earthquake, as indicated by our stress model (Figure 9), or because it already slipped in an earlier earthquake in pre-instrumental times or in an undetected slip transient on the Kyzilart Transfer Zone. That foreshock activity is at most weakly dependent on previous mainshock occurrence (Figure 2) corroborates the inference that the static stress changes contributed only little to the total stress budget of the faults. The consistency between the earthquake moment tensor and the regional stress tensor verifies that the earthquake responded to the long-term tectonic loading.

Beyond the nearfield, where ΔCFS dominates, dynamic stress changes probably play an important role to generate aftershocks (Felzer & Brodsky, 2006) or even trigger remote earthquakes (Gomberg & Johnson, 2005). But dynamic stresses act almost immediately and do not provide an explanation for the multi-month delays between the events. That the observed seismicity, both the three major sequences but also the more moderate ones, appears to occur at with time increasing distances from the Sarez earthquake rupture (Figure 2) may point at another process, namely fluid diffusion. Pore pressure counteracts normal stress and has a decisive effect on the frictional stability of faults. Faults are hydrological systems that store fluids if they are sealed and guide them if they are permeable. In sealed fault systems, fluids may be pressurized. An earthquake may breach seals and mobilize the fluids (Sibson, 1992). Brittle damage generated by the mainshock and aftershocks can increase permeability of fault zones by orders of magnitude (Kitagawa et al., 2002; Miller & Nur, 2000), particularly in the damage zones surrounding the fault cores, making them perfect transportation pathways for fluids. There is strong geophysical indication for fluids in the Pamir's upper crust that contains the fault systems discussed here: a magneto-telluric profile—traversing the Pamir near the Sary-Tash earthquake—showed high-conductivity regions across the MPTS that were interpreted as due to aqueous fluids taking up the brittle damage zones (Saß et al., 2014). This is corroborated by significantly increased P- to S-wave velocity ratios in the upper ∼10 km of the crust along the MPTS detected by tomography (Sippl, Schurr, Tympel, et al., 2013). A contribution of poro-elastic rebound is consistent with the post-seismic deformation pattern of the Sarez earthquake (Fialko et al., 2021). The fault zones that ruptured during the three major earthquakes are almost adjoining and are likely interconnected. We hypothesize that fluids captured in the fault zone of the Sarez earthquake were co-seismically freed and pressured along the SKFS where permeability may have been increased by brittle fracturing and transient stress changes (Manga et al., 2012; Fitzenz & Miller, 2001), generating aftershocks, reaching the MPTS and triggering the Sary-Tash earthquake. This may have initiated another fluid pressure wave sweeping through the fracture mesh connecting the MPTS and the Muji fault zone, eventually triggering the third event. Whether the more isolated sequences (H and I, Figure 2a) were also reached by a fluid-pressure front is unclear. The swarm-like normal faulting sequence D, coeval with the Sarez earthquake sequence as far as we can tell, may have been initiated by dynamic perturbation of the hydraulic system through transient stresses from strong shaking, as has been observed at many occasions (Manga et al., 2012).

8 Conclusion

We analyzed the seismic record of the earthquake sequence that struck the Pamir highlands in 2015–2017 in detail. Our observation started ∼4 months before the initial M_W 7.2 Sarez earthquake, for which no significant precursory seismic activity could be detected. The subsequent M_W 6.4 Sary-Tash and M_W 6.6 Muji earthquakes on adjacent faults, but more than 80 km away, showed foreshock activity, as did other M_W 4.4–5.7 earthquakes in the region. Aftershock seismicity traced the activated fault zones and testified to the plateau dissecting nature of the Sarez Karakul Fault System, interaction of the Main Pamir Thrust System with the northerly adjacent Tian Shan, and growth of the Pamir over the Tarim Basin in the east. Static stress transfer contributed at most subordinately to the stress budget of the activated fault segments. More likely, fluids migrating through the damaged fault zones triggered the subsequent earthquakes. An improved detection and quantification of such fluid processes is required to gain a better understanding of the mechanisms that trigger seismicity during periods of seismic unrest.

Acknowledgments

We thank the drivers and field participants from the Institute of Tibetan Plateau Research, especially Hongbing Liu, who helped to organize the station deployment, and Christian Sippl, Sebastian Hainzl, and Rongjiang Wang for sharing code and discussion. Funded by the CaTeNA project of the German Federal Ministry of Science and Education (support codes 03G0878A and 03G0878B) and German Research Council project RA 442/41. Seismic data was handled using *obspy* (Krischer et al., 2015) and *pyrocko* (Heimann et al., 2017). Figures were created with the help of the *Generic Mapping Tools* (Wessel et al., 2013), *maplotlib* (Hunter, 2007) and *Scientific Color Maps* (Crameri et al., 2020). Part of the instruments were provided by GIPP of GFZ Potsdam. Seismic data are archived in the GEOFON data center. The seismic event catalog will be made available through GFZ data services (`https://dataservices.gfz-potsdam.de`). LiCSAR (Looking into the Continents from Space) contains modified Copernicus Sentinel data analysed by the Centre for the Observation and Modelling of Earthquakes, Volcanoes and Tectonics (COMET; `https://comet.nerc.ac.uk/comet-lics-portal`) LiCSAR uses JASMIN, the UK's collaborative data analysis environment (`https://jasmin.ac.uk`).

References

Abdulhameed, S., Ratschbacher, L., Jonckheere, R., Gagała, Ł., Enkelmann, E., Käßner, A., ... others (2020). Tajik basin and southwestern Tian Shan, northwestern India-Asia collision zone: 2. Timing of basin inversion, Tian Shan mountain building, and relation to Pamir-plateau advance and deep India-Asia indentation. *Tectonics*, *39*(5), e2019TC005873.

Aldersons, F. (2004). Toward three-dimensional crustal structure of the Dead Sea region from local earthquake tomography. *PhD thesis*.

Arrowsmith, J. R., & Strecker, M. (1999). Seismotectonic range-front segmentation and mountain-belt growth in the Pamir-Alai region, Kyrgyzstan (India-Eurasia collision zone). *Geological Society of America Bulletin*, *111*(11), 1665–1683.

Bedford, J. R., Moreno, M., Deng, Z., Oncken, O., Schurr, B., John, T., ... Bevis, M. (2020). Months-long thousand-kilometre-scale wobbling before great subduction earthquakes. *Nature*, *580*(7805), 628–635.

Bekker, Y. A. (1996). Tectonics of the Afghan-Tajik depression. *Geotectonics*, *30*(1), 64–70.

Bie, L., Hicks, S., Garth, T., Gonzalez, P., & Rietbrock, A. (2018). 'Two go together': Near-simultaneous moment release of two asperities during the 2016 Mw 6.6 Muji, China earthquake. *Earth and Planetary Science Letters*, *491*, 34–42. doi: 10.1016/j.epsl.2018.03.033

Bloch, W., Schurr, B., Yuan, X., Ratschbacher, L., Reuter, S., Kufner, S., . . . Zhao, J. (2021, April). Structure and stress field of the deep lithosphere between Pamir and Tarim. *EarthArXiv preprint*. Retrieved from `https://doi.org/10.31223/x5n60c` doi: 10.31223/x5n60c

Bormann, P., & Dewey, J. W. (2012). The new IASPEI standards for determining magnitudes from digital data and their relation to classical magnitudes. In *New Manual of Seismological Observatory Practice 2 (NMSOP-2)* (pp. 1–44). Deutsches GeoForschungsZentrum GFZ.

Bouchon, M. (1981). A simple method to calculate Green's functions for elastic layered media. *Bulletin of the Seismological Society of America*, *71*(4), 959–971.

Chen, K., Avouac, J.-P., Aati, S., Milliner, C., Zheng, F., & Shi, C. (2020). Cascading and pulse-like ruptures during the 2019 Ridgecrest earthquakes in the Eastern California Shear Zone. *Nature communications*, *11*(1), 1–8.

Chevalier, M.-L., Pan, J., Li, H., Liu, D., & Wang, M. (2015). Quantification of both normal and right-lateral late Quaternary activity along the Kongur Shan extensional system, Chinese Pamir. *Terra Nova*, *27*(5), 379–391.

Cocco, M., & Rice, J. R. (2002). Pore pressure and poroelasticity effects in Coulomb stress analysis of earthquake interactions. *Journal of Geophysical Research: Solid Earth*, *107*(B2), ESE–2.

Comino, J. Á. L., Heimann, S., Cesca, S., Milkereit, C., Dahm, T., & Zang, A. (2017). Automated full waveform detection and location algorithm of acoustic emissions from hydraulic fracturing experiment. *Procedia engineering*, *191*, 697–702.

Cowgill, E. (2010). Cenozoic right-slip faulting along the eastern margin of the Pamir salient, northwestern China. *Bulletin*, *122*(1-2), 145–161.

Crameri, F., Shephard, G. E., & Heron, P. J. (2020). The misuse of colour in science communication. *Nature communications*, *11*(1), 1–10.

Das, S., & Henry, C. (2003). Spatial relation between main earthquake slip and its aftershock distribution. *Reviews of Geophysics*, *41*(3).

Diehl, T., Deichmann, N., Kissling, E., & Husen, S. (2009). Automatic S-wave picker for local earthquake tomography. *Bulletin of the Seismological Society of America*, *99*(3), 1906–1920.

Di Giacomo, D., Engdahl, E. R., & Storchak, D. A. (2018). The ISC-GEM earthquake catalogue (1904–2014): status after the extension project. *Earth System Science Data*, *10*(4), 1877–1899.

Elliott, A., Elliott, J., Hollingsworth, J., Kulikova, G., Parsons, B., & Walker, R. (2020). Satellite imaging of the 2015 M 7.2 earthquake in the Central Pamir, Tajikistan, elucidates a sequence of shallow strike-slip ruptures of the Sarez-Karakul fault. *Geophysical Journal International*, *221*(3), 1696–1718.

Ellsworth, W. L., & Bulut, F. (2018). Nucleation of the 1999 Izmit earthquake by a triggered cascade of foreshocks. *Nature Geoscience*, *11*(7), 531–535.

Felzer, K. R., & Brodsky, E. E. (2006). Decay of aftershock density with distance indicates triggering by dynamic stress. *Nature*, *441*(7094), 735–738.

Fialko, Y., Jin, Z., Zubovich, A., & Schöne, T. (2021). Lithospheric deformation due to the 2015 M7.2 Sarez (Pamir) earthquake constrained by 5 years of space geodetic observations. *Earth and Space Science Open Archive*, 49. Retrieved from `https://doi.org/10.1002/essoar.10508106.1` doi: 10.1002/essoar.10508106.1

Fitzenz, D. D., & Miller, S. A. (2001). A forward model for earthquake generation on interacting faults including tectonics, fluids, and stress transfer. *Journal of Geophysical Research: Solid Earth*, *106*(B11), 26689–26706.

Freed, A. M., & Lin, J. (2001). Delayed triggering of the 1999 Hector Mine earthquake by viscoelastic stress transfer. *Nature*, *411*(6834), 180–183.

Gagała, Ł., Ratschbacher, L., Ringenbach, J.-C., Kufner, S.-K., Schurr, B., Dedow, R., ... Oimahmadov, I. (2020). Tajik Basin and Southwestern Tian Shan, Northwestern India-Asia Collision Zone: 1. Structure, Kinematics, and Salt Tectonics in the Tajik Fold-and-Thrust Belt of the Western Foreland of the Pamir. *Tectonics*, *39*(5), e2019TC005871.

Gephart, J. W., & Forsyth, D. W. (1984). An improved method for determining the regional stress tensor using earthquake focal mechanism data: application to the San Fernando earthquake sequence. *Journal of Geophysical Research: Solid Earth*, *89*(B11), 9305–9320.

Gomberg, J., & Johnson, P. (2005). Dynamic triggering of earthquakes. *Nature*, *437*(7060), 830–830.

Harris, R. A. (1998). Introduction to special section: Stress triggers, stress shadows, and implications for seismic hazard. *Journal of Geophysical Research: Solid Earth*, *103*(B10), 24347–24358.

He, P., Hetland, E. A., Niemi, N. A., Wang, Q., Wen, Y., & Ding, K. (2018). The 2016 Mw 6.5 Nura earthquake in the Trans Alai range, northern Pamir: possible rupture on a back-thrust fault constrained by Sentinel-1A radar interferometry. *Tectonophysics*, *749*, 62–71.

Heimann, S., Kriegerowski, M., Isken, M., Cesca, S., Daout, S., Grigoli, F., ... others (2017). Pyrocko-An open-source seismology toolbox and library. *GFZ Data Services*.

Hooper, A. (2008). A multi-temporal InSAR method incorporating both persistent scatterer and small baseline approaches. *Geophysical Research Letters*, *35*(16).

Hunter, J. D. (2007). Matplotlib: A 2D graphics environment. *Computing in Science & Engineering*, *9*(3), 90–95. doi: 10.1109/MCSE.2007.55

ISC. (2021). *ISC-GEM Earthquake Catalogue* (Tech. Rep.). International Seismological Centre. doi: https://doi.org/10.31905/d808b825

Ischuk, A., Bendick, R., Rybin, A., Molnar, P., Khan, S. F., Kuzikov, S., ... others (2013). Kinematics of the Pamir and Hindu Kush regions from GPS geodesy. *Journal of geophysical research: solid earth*, *118*(5), 2408–2416.

Isken, M., Sudhaus, H., Heimann, S., Steinberg, A., Daout, S., & Vasyura-Bathke, H. (2017). Kite-software for rapid earthquake source optimisation from insar surface displacement. *GFZ Data Services*. doi: 10.5880/GFZ.2.1.2017.002

Jade, S., Bhatt, B., Yang, Z., Bendick, R., Gaur, V., Molnar, P., ... Kumar, D. (2004). GPS measurements from the Ladakh Himalaya, India: Preliminary tests of plate-like or continuous deformation in Tibet. *Geological Society of America Bulletin*, *116*(11-12), 1385–1391.

Käßner, A., Ratschbacher, L., Jonckheere, R., Enkelmann, E., Khan, J., Sonntag, B.-L., ... Oimahmadov, I. (2016). Cenozoic intracontinental deformation and exhumation at the northwestern tip of the India-Asia collision—southwestern Tian Shan, Tajikistan, and Kyrgyzstan. *Tectonics*, *35*(9), 2171–2194.

Kissling, E., Ellsworth, W., Eberhart-Phillips, D., & Kradolfer, U. (1994). Initial reference models in local earthquake tomography. *Journal of Geophysical Research: Solid Earth*, *99*(B10), 19635–19646.

Kitagawa, Y., Fujimori, K., & Koizumi, N. (2002). Temporal change in permeability of the rock estimated from repeated water injection experiments near the Nojima fault in Awaji Island, Japan. *Geophysical research letters*, *29*(10), 121–1.

Kreemer, C., Blewitt, G., & Klein, E. C. (2014). A geodetic plate motion and Global Strain Rate Model. *Geochemistry, Geophysics, Geosystems*, *15*(10), 3849–3889.

Krischer, L., Megies, T., Barsch, R., Beyreuther, M., Lecocq, T., Caudron, C., & Wassermann, J. (2015). ObsPy: A bridge for seismology into the scientific Python ecosystem. *Computational Science & Discovery*, *8*(1), 014003.

Kufner, S.-K., Kakar, N., Bezada, M., Bloch, W., Metzger, S., Yuan, X., … others (2021). The Hindu Kush slab break-off as revealed by deep structure and crustal deformation. *Nature communications*, *12*(1), 1–11.

Kufner, S.-K., Schurr, B., Haberland, C., Zhang, Y., Saul, J., Ischuk, A., & Oimahmadov, I. (2017). Zooming into the Hindu Kush slab break-off: A rare glimpse on the terminal stage of subduction. *Earth and Planetary Science Letters*, *461*, 127–140.

Kufner, S.-K., Schurr, B., Ratschbacher, L., Murodkulov, S., Abdulhameed, S., Ischuk, A., … Kakar, N. (2018). Seismotectonics of the Tajik basin and surrounding mountain ranges. *Tectonics*, *37*(8), 2404–2424.

Kufner, S.-K., Schurr, B., Sippl, C., Yuan, X., Ratschbacher, L., Ischuk, A., … others (2016). Deep India meets deep Asia: Lithospheric indentation, delamination and break-off under Pamir and Hindu Kush (Central Asia). *Earth and Planetary Science Letters*, *435*, 171–184.

Kulikova, G., Schurr, B., Krüger, F., Brzoska, E., & Heimann, S. (2016). Source parameters of the Sarez-Pamir earthquake of 1911 February 18. *Geophysical Journal International*, *205*(2), 1086–1098.

Lazecky, M., Spaans, K., González, P. J., Maghsoudi, Y., Morishita, Y., Albino, F., … others (2020). LiCSAR: An Automatic InSAR Tool for Measuring and Monitoring Tectonic and Volcanic Activity. *Remote Sensing*.

Lee, W. H. K., & Lahr, J. C. (1972). *HYPO71: A computer program for determin-*

ing hypocenter, magnitude, and first motion pattern of local earthquakes. US Department of the Interior, Geological Survey, National Center for . . . .

Li, J., Liu, G., Qiao, X., Xiong, W., Liu, D., Sun, J., . . . others (2019). Rupture characteristics of the 25 November 2016 Aketao earthquake (M w 6.6) in eastern Pamir revealed by GPS and teleseismic data. In *Earthquakes and Multi-hazards Around the Pacific Rim, Vol. II* (pp. 49–61). Springer.

Li, T., Schoenbohm, L. M., Chen, J., Yuan, Z., Feng, W., Li, W., . . . others (2019). Cumulative and Coseismic (During the 2016 Mw 6.6 Aketao Earthquake) Deformation of the Dextral-Slip Muji Fault, Northeastern Pamir Orogen. *Tectonics*, *38*(11), 3975–3989.

Manga, M., Beresnev, I., Brodsky, E. E., Elkhoury, J. E., Elsworth, D., Ingebritsen, S. E., . . . Wang, C.-Y. (2012). Changes in permeability caused by transient stresses: Field observations, experiments, and mechanisms. *Reviews of Geophysics*, *50*(2).

Metzger, S., Ischuk, A., Deng, Z., Ratschbacher, L., Perry, M., Kufner, S.-K., . . . Moreno, M. (2020). Dense GNSS profiles across the northwestern tip of the India-Asia collision zone: Triggered slip and westward flow of the Peter the First Range, Pamir, into the Tajik Depression. *Tectonics*, *39*(2), e2019TC005797.

Metzger, S., Schurr, B., Ratschbacher, L., Sudhaus, H., Kufner, S.-K., Schöne, T., . . . Bendick, R. (2017). The 2015 Mw7. 2 Sarez Strike-Slip Earthquake in the Pamir Interior: Response to the Underthrusting of India's Western Promontory. *Tectonics*, *36*(11), 2407–2421.

Michael, A. J. (1984). Determination of stress from slip data: faults and folds. *Journal of Geophysical Research: Solid Earth*, *89*(B13), 11517–11526.

Michael, A. J. (1987). Use of focal mechanisms to determine stress: a control study. *Journal of Geophysical Research: Solid Earth*, *92*(B1), 357–368.

Mildon, Z., Roberts, G. P., Walker, J. F., & Toda, S. (2019). Coulomb pre-stress and fault bends are ignored yet vital factors for earthquake triggering and hazard. *Nature communications*, *10*(1), 1–9.

Miller, S. A., & Nur, A. (2000). Permeability as a toggle switch in fluid-controlled crustal processes. *Earth and Planetary Science Letters*, *183*(1-2), 133–146.

Morishita, Y., Lazecky, M., Wright, T. J., Weiss, J. R., Elliott, J. R., & Hooper,

A. (2020). LiCSBAS: An Open-Source InSAR Time Series Analysis Package Integrated with the LiCSAR Automated Sentinel-1 InSAR Processor. *Remote Sensing*, *12*(3), 424.

Nábělek, J., & Xia, G. (1995). Moment-tensor analysis using regional data: Application to the 25 March, 1993, Scotts Mills, Oregon, Earthquake. *Geophysical Research Letters*, *22*(1), 13–16.

Nöth, L. (1932). *Geologische Untersuchungen im nordwestlichen Pamirgebiet und mittleren Transalai.* D. Reimer, E. Vohsen.

Okada, Y. (1985). Surface deformation due to shear and tensile faults in a half-space. *Bulletin of the seismological society of America*, *75*(4), 1135–1154.

Perry, M., Kakar, N., Ischuk, A., Metzger, S., Bendick, R., Molnar, P., & Mohadjer, S. (2019). Little geodetic evidence for localized Indian subduction in the Pamir-Hindu Kush of Central Asia. *Geophysical Research Letters*, *46*(1), 109–118.

PMP International (Tajikistan). (2005). Tajikistan National Seismic Network [Computer software manual]. doi: doi:10.7914/SN/TJ

Pozzi, J.-P., & Feinberg, H. (1991). Paleomagnetism in the Tajikistan: Continental shortening of European margin in the Pamirs during Indian Eurasian collision. *Earth and Planetary Science Letters*, *103*(1-4), 365–378.

Qiao, X., Wang, Q., Yang, S., Li, J., Zou, R., & Ding, K. (2015). The 2008 Nura Mw6. 7 earthquake: A shallow rupture on the Main Pamir Thrust revealed by GPS and InSAR. *Geodesy and Geodynamics*, *6*(2), 91–100. doi: 10.1016/j.geog.2015.01.005

Rice, J. R., & Cleary, M. P. (1976). Some basic stress diffusion solutions for fluid-saturated elastic porous media with compressible constituents. *Reviews of Geophysics*, *14*(2), 227–241.

Robinson, A. C. (2009). Geologic offsets across the northern Karakorum fault: Implications for its role and terrane correlations in the western Himalayan-Tibetan orogen. *Earth and Planetary Science Letters*, *279*(1-2), 123–130.

Robinson, A. C., Yin, A., Manning, C. E., Harrison, T. M., Zhang, S.-H., & Wang, X.-F. (2004). Tectonic evolution of the northeastern Pamir: Constraints from the northern portion of the Cenozoic Kongur Shan extensional system, western China. *Geological Society of America Bulletin*, *116*(7-8), 953–973.

Robinson, A. C., Yin, A., Manning, C. E., Harrison, T. M., Zhang, S.-H., & Wang, X.-F. (2007). Cenozoic evolution of the eastern Pamir: Implications for strain-accommodation mechanisms at the western end of the Himalayan-Tibetan orogen. *Geological Society of America Bulletin*, *119*(7-8), 882–896.

Rutte, D., Ratschbacher, L., Schneider, S., Stübner, K., Stearns, M. A., Gulzar, M. A., & Hacker, B. R. (2017). Building the Pamir-Tibetan Plateau—Crustal stacking, extensional collapse, and lateral extrusion in the Central Pamir: 1. Geometry and kinematics. *Tectonics*, *36*(3), 342–384.

Ryder, I., Bürgmann, R., & Fielding, E. (2012). Static stress interactions in extensional earthquake sequences: An example from the South Lunggar Rift, Tibet. *Journal of Geophysical Research: Solid Earth*, *117*(B9).

Sangha, S., Peltzer, G., Zhang, A., Meng, L., Liang, C., Lundgren, P., & Fielding, E. (2017). Fault geometry of 2015, Mw7. 2 Murghab, Tajikistan earthquake controls rupture propagation: Insights from InSAR and seismological data. *Earth and Planetary Science Letters*, *462*, 132–141.

Saß, P., Ritter, O., Ratschbacher, L., Tympel, J., Matiukov, V., Rybin, A., & Batalev, V. Y. (2014). Resistivity structure underneath the Pamir and southern Tian Shan. *Geophysical Journal International*, *198*(1), 564–579.

Schneider, F., Yuan, X., Schurr, B., Mechie, J., Sippl, C., Haberland, C., … others (2013). Seismic imaging of subducting continental lower crust beneath the Pamir. *Earth and Planetary Science Letters*, *375*, 101–112.

Schurr, B., Moreno, M., Tréhu, A. M., Bedford, J., Kummerow, J., Li, S., & Oncken, O. (2020). Forming a Mogi doughnut in the years prior to and immediately before the 2014 M8. 1 Iquique, northern Chile, earthquake. *Geophysical Research Letters*, *47*(16), e2020GL088351.

Schurr, B., Ratschbacher, L., Sippl, C., Gloaguen, R., Yuan, X., & Mechie, J. (2014). Seismotectonics of the Pamir. *Tectonics*, *33*(8), 1501–1518.

SEISDMC. (2021). Data management centre of the China National Seismic Network at the Institute of Geophysics. *China Earthquake Administration*. doi: 10.11998/SeisDmc/SN

Sibson, R. (1992). Implications of fault-valve behaviour for rupture nucleation and recurrence. *Tectonophysics*, *211*(1-4), 283–293.

Sippl, C., Ratschbacher, L., Schurr, B., Krumbiegel, C., Rui, H., Pingren, L., & Abdybachaev, U. (2014). The 2008 Nura earthquake sequence at the Pamir-Tian Shan collision zone, southern Kyrgyzstan. *Tectonics*, *33*(12), 2382–2399.

Sippl, C., Schurr, B., Tympel, J., Angiboust, S., Mechie, J., Yuan, X., … others (2013). Deep burial of Asian continental crust beneath the Pamir imaged with local earthquake tomography. *Earth and Planetary Science Letters*, *384*, 165–177.

Sippl, C., Schurr, B., Yuan, X., Mechie, J., Schneider, F., Gadoev, M., … others (2013). Geometry of the Pamir-Hindu Kush intermediate-depth earthquake zone from local seismic data. *Journal of Geophysical Research: Solid Earth*, *118*(4), 1438–1457.

Sobel, E. R., Schoenbohm, L. M., Chen, J., Thiede, R., Stockli, D. F., Sudo, M., & Strecker, M. R. (2011). Late Miocene–Pliocene deceleration of dextral slip between Pamir and Tarim: Implications for Pamir orogenesis. *Earth and Planetary Science Letters*, *304*(3-4), 369–378.

Stein, R. S. (1999). The role of stress transfer in earthquake occurrence. *Nature*, *402*(6762), 605–609.

Strecker, M., Frisch, W., Hamburger, M., Ratschbacher, L., Semiletkin, S., Zamoruyev, A., & Sturchio, N. (1995). Quaternary deformation in the eastern Pamirs, Tadzhikistan and Kyrgyzstan. *Tectonics*, *14*(5), 1061–1079.

Strom, A. (2014). Sarez Lake problem: ensuring long-term safety. In *Landslide Science for a Safer Geoenvironment* (pp. 633–639). Springer.

Stübner, K., Ratschbacher, L., Rutte, D., Stanek, K., Minaev, V., Wiesinger, M., … members, P. T. (2013). The giant Shakhdara migmatitic gneiss dome, Pamir, India-Asia collision zone: 1. Geometry and kinematics. *Tectonics*, *32*(4), 948–979.

Tanaka, S., Ohtake, M., & Sato, H. (2002). Evidence for tidal triggering of earthquakes as revealed from statistical analysis of global data. *Journal of Geophysical Research: Solid Earth*, *107*(B10), ESE–1.

Tape, C., Holtkamp, S., Silwal, V., Hawthorne, J., Kaneko, Y., Ampuero, J. P., … West, M. E. (2018). Earthquake nucleation and fault slip complexity in the lower crust of central Alaska. *Nature Geoscience*, *11*(7), 536–541.

Teshebaeva, K., Sudhaus, H., Echtler, H., Schurr, B., & Roessner, S. (2014). Strain partitioning at the eastern Pamir-Alai revealed through SAR data analysis of the 2008 Nura earthquake. *Geophysical Journal International*, *198*(2), 760–774.

Thiede, R. C., Sobel, E. R., Chen, J., Schoenbohm, L. M., Stockli, D. F., Sudo, M., & Strecker, M. R. (2013). Late Cenozoic extension and crustal doming in the India-Eurasia collision zone: New thermochronologic constraints from the NE Chinese Pamir. *Tectonics*, *32*(3), 763–779.

Thomas, J.-C., Chauvin, A., Gapais, D., Bazhenov, M., Perroud, H., Cobbold, P., & Burtman, V. (1994). Paleomagnetic evidence for Cenozoic block rotations in the Tadjik depression (Central Asia). *Journal of Geophysical Research: Solid Earth*, *99*(B8), 15141–15160.

Thurber, C. H. (1983). Earthquake locations and three-dimensional crustal structure in the Coyote Lake area, central California. *Journal of Geophysical Research: Solid Earth*, *88*(B10), 8226–8236.

Toda, S., & Stein, R. S. (2020). Long-and short-term stress interaction of the 2019 Ridgecrest sequence and Coulomb-based earthquake forecasts. *Bulletin of the Seismological Society of America*, *110*(4), 1765–1780.

Toda, S., Stein, R. S., Reasenberg, P. A., Dieterich, J. H., & Yoshida, A. (1998). Stress transferred by the 1995 Mw= 6.9 Kobe, Japan, shock: Effect on aftershocks and future earthquake probabilities. *Journal of Geophysical Research: Solid Earth*, *103*(B10), 24543–24565.

Waldhauser, F., & Ellsworth, W. L. (2000). A double-difference earthquake location algorithm: Method and application to the northern Hayward fault, California. *Bulletin of the Seismological Society of America*, *90*(6), 1353–1368.

Wang, R., Lorenzo-Martin, F., & Roth, F. (2006). PSGRN/PSCMP—a new code for calculating co-and post-seismic deformation, geoid and gravity changes based on the viscoelastic-gravitational dislocation theory. *Computers & Geosciences*, *32*(4), 527–541.

Wells, D. L., & Coppersmith, K. J. (1994). New empirical relationships among magnitude, rupture length, rupture width, rupture area, and surface displacement. *Bulletin of the seismological Society of America*, *84*(4), 974–1002.

Wessel, P., Smith, W. H., Scharroo, R., Luis, J., & Wobbe, F. (2013). Generic mapping tools: improved version released. *Eos, Transactions American Geophysical Union*, *94*(45), 409–410.

Worthington, J. R., Ratschbacher, L., Stübner, K., Khan, J., Malz, N., Schneider, S., ... others (2020). The Alichur dome, South Pamir, western India–Asia collisional zone: Detailing the Neogene Shakhdara–Alichur syn-collisional gneiss-dome complex and connection to lithospheric processes. *Tectonics*, *39*(1), e2019TC005735.

Yu, C., Li, Z., Penna, N. T., & Crippa, P. (2018). Generic atmospheric correction model for Interferometric Synthetic Aperture Radar observations. *Journal of Geophysical Research: Solid Earth*, *123*(10), 9202–9222.

Yuan, X., Schurr, B., Bloch, W., Xu, Q., & Zhao, J. (2018). East Pamir. *GFZ Data services*.

Yuan, X., Schurr, B., Kufner, S.-K., & Bloch, W. (2018). Sarez Pamir aftershock seismic network. *GFZ Data services*.

Yushin, I., Sass, M., Karapetov, S., Altukhov, S., Teplov, I., Raeakov, C., ... Davidchenko, A. (1964). 1: 200,000 maps of the Tajik SSR. *Russian Geological Research Institute*.

Zhou, Y., He, J., Oimahmadov, I., Gadoev, M., Pan, Z., Wang, W., ... Rajabov, N. (2016). Present-day crustal motion around the Pamir Plateau from GPS measurements. *Gondwana Research*, *35*, 144–154.

Zubovich, A. V., Schöne, T., Metzger, S., Mosienko, O., Mukhamediev, S., Sharshebaev, A., & Zech, C. (2016). Tectonic interaction between the Pamir and Tien Shan observed by GPS. *Tectonics*, *35*(2), 283–292.

Zubovich, A. V., Wang, X.-q., Scherba, Y. G., Schelochkov, G. G., Reilinger, R., Reigber, C., ... others (2010). GPS velocity field for the Tien Shan and surrounding regions. *Tectonics*, *29*(6).

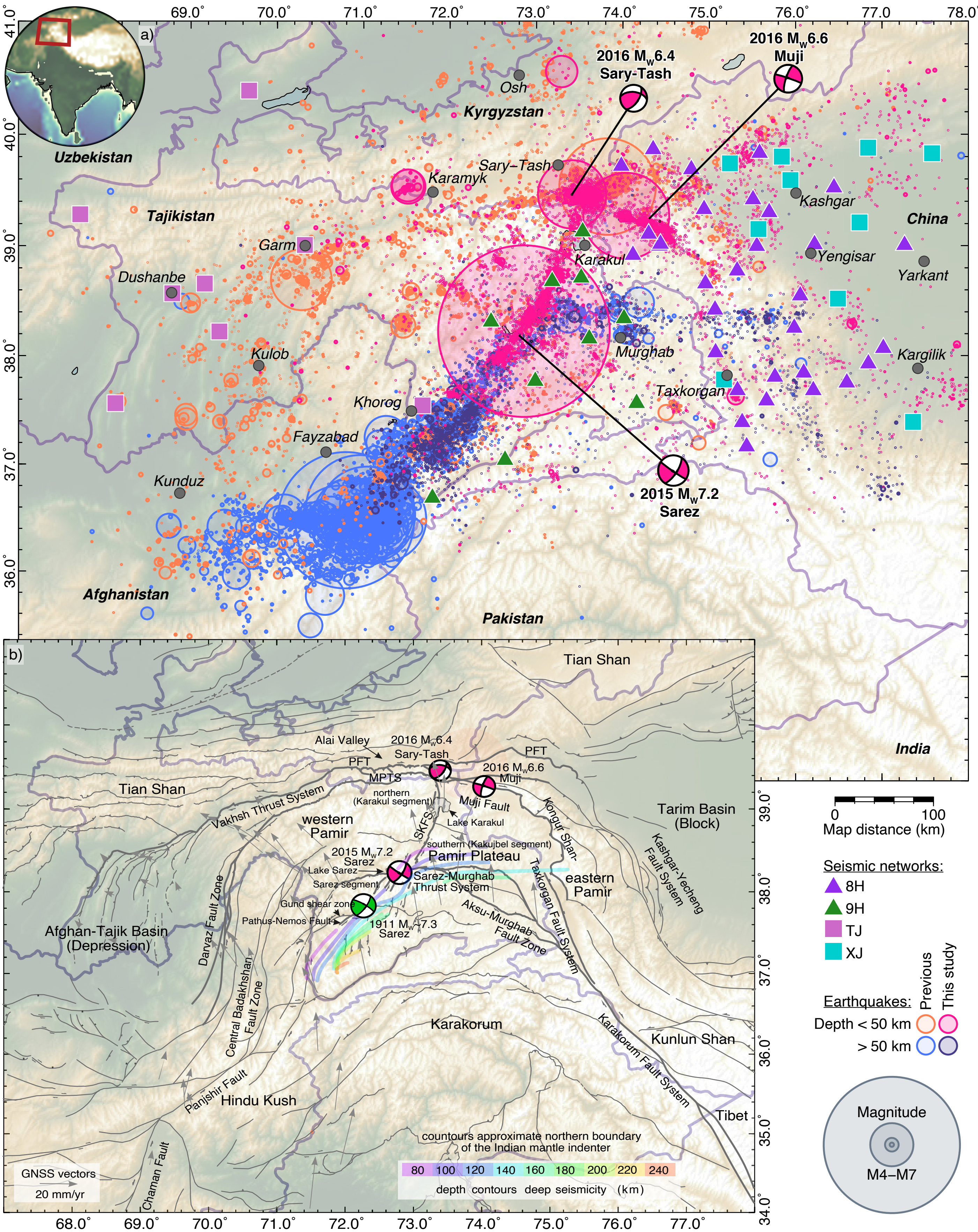
a)
2016 Mw6.4
Sary-Tash
2016 Mw6.6
Muji
2015 Mw7.2
Sarez
Osh
Kyrgyzstan
Uzbekistan
Tajikistan
Karamyk
Sary–Tash
Kashgar
China
Garm
Karakul
Yengisar
Yarkant
Dushanbe
Murghab
Kargilik
Kulob
Taxkorgan
Khorog
Fayzabad
Kunduz
Afghanistan
Pakistan
India
b)
Tian Shan
Alai Valley
PFT
MPTS
northern (Karakul segment)
Muji Fault
Lake Karakul
Vakhsh Thrust System
western Pamir
SKFS
southern (Kakujbel segment)
Pamir Plateau
Kongur Shan
Tarim Basin (Block)
Kashgar-Yecheng Fault System
Lake Sarez
Sarez segment
Sarez-Murghab Thrust System
eastern Pamir
Taxkorgan Fault System
Gund shear zone
Pathus-Nemos Fault
1911 Mw~7.3 Sarez
Aksu-Murghab Fault Zone
Afghan-Tajik Basin (Depression)
Darvaz Fault Zone
Central Badakhshan Fault Zone
Karakorum
Kunlun Shan
Karakorum Fault System
Panjshir Fault
Hindu Kush
Tibet
Chaman Fault
countours approximate northern boundary of the Indian mantle indenter
80 100 120 140 160 180 200 220 240
depth contours deep seismicity (km)
GNSS vectors
20 mm/yr
0 100
Map distance (km)
Seismic networks:
8H
9H
TJ
XJ
Earthquakes:
Previous
This study
Depth < 50 km
> 50 km
Magnitude
M4–M7

Figure 1. (a) Location of the study area, seismic stations, seismicity from this and previous (Schurr et al., 2014; Kufner et al., 2017, 2018) studies, and moment tensors of the three largest earthquakes of the sequence. Crustal seismicity (depth$<$50 km) delineates the active fault zones. Intermediate depth seismicity (depth$>$50 km) indicates subduction of Indian lithosphere beneath the Hindu Kush (Kufner et al., 2017, 2021) and delamination of Asian lithosphere beneath the Pamir (Sippl, Schurr, Yuan, et al., 2013; Bloch et al., 2021). (b) Tectonic map of the Cenozoic faults with the neotectonic faults discussed in the text highlighted and named. Focal mechanism of the 1911 Sarez earthquake is from Kulikova et al. (2016) and its location follows Elliott et al. (2020). Depth contours of intermediate-depth seismicity are from Schurr et al. (2014). Global Navigation Satellite System (GNSS) displacement rates from the Pamir Plateau and is western foreland are from Perry et al. (2019).

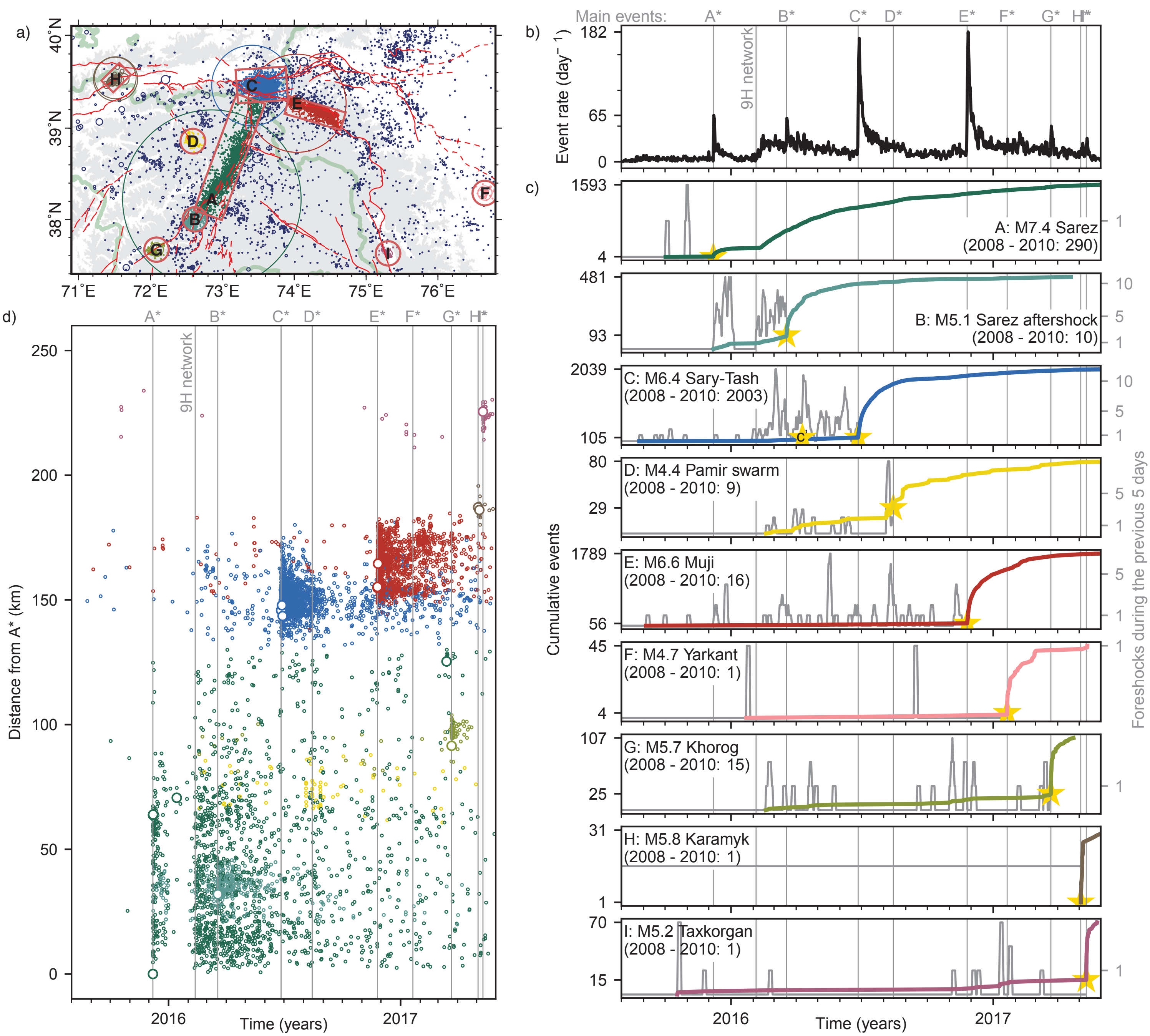
a)
b)
c)
d)
Main events: A* B* C* D* E* F* G* H* I*
9H network
Event rate (day^{-1})
A: M7.4 Sarez
(2008 - 2010: 290)
B: M5.1 Sarez aftershock
(2008 - 2010: 10)
C: M6.4 Sary-Tash
(2008 - 2010: 2003)
D: M4.4 Pamir swarm
(2008 - 2010: 9)
E: M6.6 Muji
(2008 - 2010: 16)
F: M4.7 Yarkant
(2008 - 2010: 1)
G: M5.7 Khorog
(2008 - 2010: 15)
H: M5.8 Karamyk
(2008 - 2010: 1)
I: M5.2 Taxkorgan
(2008 - 2010: 1)
Cumulative events
Foreshocks during the previous 5 days
Distance from A* (km)
Time (years)

Figure 2. Spatio-temporal evolution of seismic activity. (a) Spatial definitions of sequences (A to I) with earthquakes color-coded as in the other subfigures and Figure 7; red lines denote major active faults. (b) Event rate of the entire catalog. (c) Cumulative event number inside each sequence (colored) and 5-day moving window event number before the mainshock for each sequence (gray); event with largest magnitude in sequence is marked with a star and labeled on top. The number in the sequence of the strongest and the last event is labeled on the left. Cumulative event number from 2008 to 2010 for the specific region in parenthesis from Schurr et al. (2014). For aftershock event rate, see Figure S4. (d) Spatial and temporal distribution of the seismic events with respect to the hypocenter of the M_W7.2 Sarez earthquake. $M_W > 5$ events are highlighted as larger circles. Most of the future mainshock volumes show foreshock activity, but foreshock activity is independent of mainshocks on other faults.

Table 1. Source parameters and failure stresses of the large and moderate earthquakes for which a moment tensor is available. Strike, dip and rake of our preferred fault plane. # denotes our moment tensors shown in Figure 7 (#s *1* and *29* are outside the map region. No # marks moment tensor from references in the footnote); sequence (Seq.) denotes the studied earthquake sequence, defined in Figure 2; * denotes the largest earthquake of the sequence. Depth is centroid depth, except for the three largest mainshocks, for which we report our hypocentral depths. The change in Coulomb failure stress (ΔCFS) is due to all previous earthquakes. For c' and C* ΔCFS without possible creep on the SKFS (Figure 4) is given in parenthesis.

#	Seq.	Time	M_W	Lon. (°E)	Lat. (°N)	Depth (km)	Strike/Dip/Rake (°)	ΔCFS (kPa)
1		2015-11-17 17:29:33	5.3	40.556	73.290	18	93/55/132	0^{+0}_{-0}
	A*	2015-12-07 07:50:04	7.2[a]	72.853	38.223	0.9	214/83/8[a]	0^{+0}_{-0}
2	A	2015-12-07 10:34:19	4.3	72.904	38.289	9.0	23/79/20	-287^{+70}_{-167}
3	A	2015-12-07 15:23:54	4.5	73.225	38.719	4.0	197/38/337	-204^{+106}_{-142}
4	B	2015-12-27 23:05:28	3.9	72.697	38.069	6.0	181/40/234	$+27^{+52}_{-34}$
5	A	2016-01-13 21:37:35	4.5	73.322	38.742	9.0	222/42/346	$+113^{+58}_{-32}$
6	B*	2016-03-18 16:10:57	5.1	72.618	38.003	4.0	221/67/9	$+130^{+54}_{-25}$
7	B	2016-03-21 05:32:26	3.8	72.581	38.002	4.0	230/37/325	-126^{+34}_{-60}
8	c'	2016-04-09 16:19:26	4.2	73.502	39.428	9.0	81/52/166	$+5^{+1}_{-1}$ $(+11^{+3}_{-2})^{d}$
	C*	2016-06-26 11:17:08	6.4[a]	73.411	39.462	11.9	266/67/126[b]	$+5^{+3}_{-1}$ $(+4^{+2}_{-2})^{d}$
9	C	2016-06-27 06:25:36	4.2	73.463	39.438	12.0	280/55/127	-386^{+121}_{-267}
10	C	2016-06-27 07:34:11	3.9	73.657	39.447	9.0	124/38/203	$+779^{+314}_{-195}$
11	C	2016-06-27 19:28:47	4.5	73.544	39.441	15.0	263/33/91	-1986^{+558}_{-526}
12	C	2016-06-28 12:43:13	4.4	73.499	39.456	15.0	290/28/179	-500^{+202}_{-393}
13	C	2016-06-28 21:38:02	5.1	73.412	39.440	15.0	90/77/161	$+34^{+154}_{-178}$
14	C	2016-06-29 08:08:12	4.3	73.471	39.443	12.0	289/55/138	-348^{+168}_{-240}
15	A	2016-06-30 07:09:40	4.0	72.930	38.426	15.0	212/71/310	-1064^{+237}_{-262}
16	C	2016-07-01 11:01:12	3.8	73.733	39.449	6.0	143/30/241	$+285^{+111}_{-75}$
17	C	2016-07-04 02:24:17	4.2	73.525	39.446	9.0	309/81/186	$+44^{+59}_{-60}$
18	A	2016-07-08 12:10:24	3.8	72.840	38.085	6.0	47/86/306	-89^{+88}_{-73}
19	C	2016-07-21 05:29:18	4.2	73.527	39.450	6.0	122/30/158	-104^{+35}_{-72}
20	D	2016-08-04 21:34:32	3.7	72.568	38.877	6.0	339/63/248	$+22^{+10}_{-5}$
21	D	2016-08-04 23:42:08	4.1	72.548	38.868	6.0	343/67/254	$+17^{+9}_{-4}$
22	D*	2016-08-14 15:05:19	4.4	72.590	38.858	6.0	332/71/237	$+15^{+10}_{-4}$
23	D	2016-08-14 15:11:35	3.9	72.584	38.838	6.0	21/62/287	$+58^{+21}_{-17}$
24	e'	2016-11-25 14:18:59	4.8	74.034	39.267	15.0	289/65/172	-13^{+4}_{-6}
	E*	2016-11-25 14:24:27	6.6[a]	74.039	39.269	13.7	106/88/184[c]	$+60^{+64}_{-71}$
25	E	2016-11-25 19:46:17	4.0	74.295	39.198	6.0	298/73/210	-1652^{+425}_{-836}
26	E	2016-11-26 09:23:22	4.6	74.274	39.202	6.0	292/79/222	-1103^{+276}_{-431}
27	E	2016-12-19 10:57:24	4.1	74.047	39.256	15.0	288/54/165	-700^{+239}_{-339}
28	F*	2017-01-20 09:54:03	4.7	76.653	38.292	12.0	189/28/143	0^{+0}_{-0}
29		2017-02-21 10:24:48	3.9	70.108	39.167	18.0	266/50/127	$+1^{+0}_{-0}$
30	A	2017-03-14 11:07:08	4.6	73.455	39.249	12.0	191/85/355	$+25^{+13}_{-10}$
31	G*	2017-03-22 11:27:01	4.6	72.084	37.668	12.0	234/85/3	$+14^{+2}_{-3}$
32	H*	2017-05-03 04:46:53	5.7	71.510	39.542	18.0	249/79/178	-3^{+1}_{-0}
33	H	2017-05-05 05:09:34	5.4	71.514	39.532	12.0	226/45/102	$+34^{+32}_{-14}$
34	I*	2017-05-10 21:58:20	5.2	75.305	37.627	6.0	320/61/254	0^{+0}_{-0}
35	C	2017-05-22 09:23:05	4.3	73.645	39.409	6.0	258/25/143	$+1409^{+527}_{-403}$

[a]NEIC; [b]He et al. (2018); [c]Bie et al. (2018); [d] without creep (Figure 4)

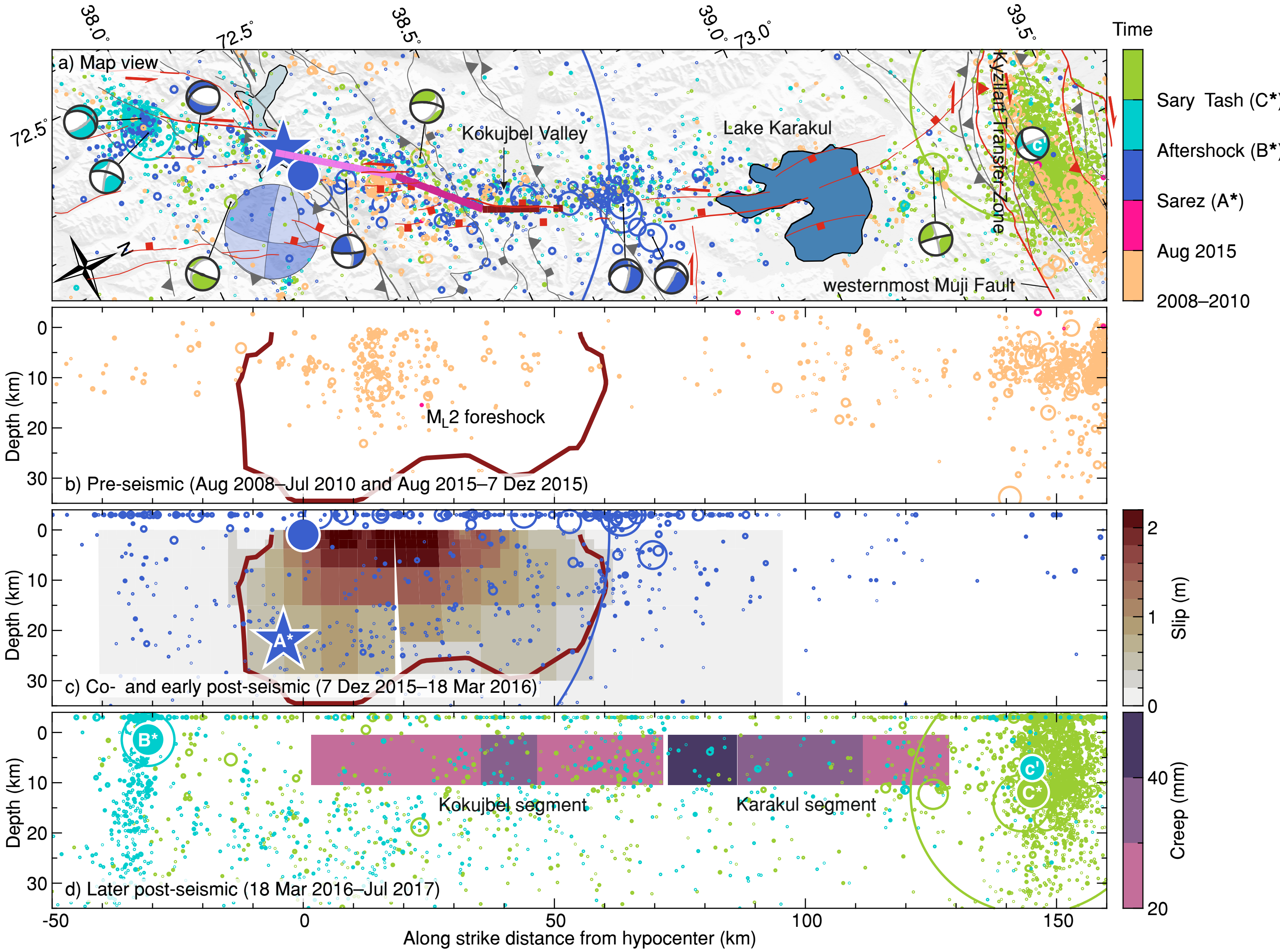

Figure 3. Time succession of seismicity and moment tensors of moderate earthquakes in the active part of the Sarez-Karakul Fault Zone; GEOFON focal mechanism (large beach ball); preferred hypocenter location by NEIC (star); 2008–2010 seismicity from Schurr et al. (2014). (a) Along-strike map view with the three segments of the co-seismic rupture highlighted (Metzger et al., 2017). Mapped Cenozoic structures in gray and neotectonic structures in red. (b–d) Along strike profiles. (b) Seismicity before the Sarez mainshock. 10% of maximum future slip contoured. (c) Early aftershock seismicity until aftershock $B*$. Co-seismic slip from Metzger et al. (2017). (d) Later aftershock seismicity. Cumulative creep model as in Figure 4 between $A*$ and $C*$ (Table 1). No significant immediate foreshock activity was detected for the Sarez earthquake. The rupture plane has been constantly active throughout 2008–2010. Aftershock seismicity skirts around the co-seismic slip patch.

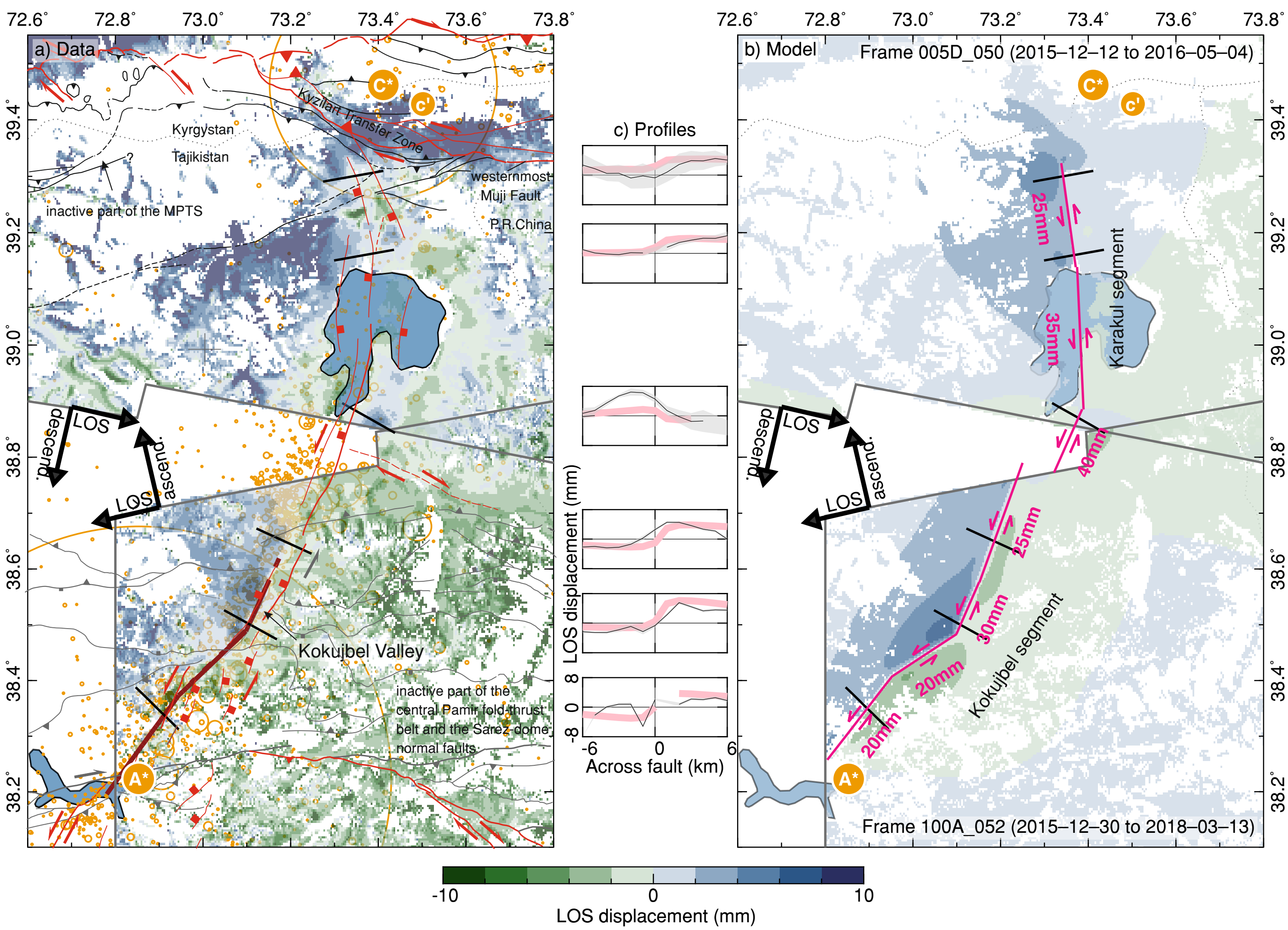

Figure 4. Post-seismic displacement on the Sarez-Karakul Fault System. (a) InSAR displacement map derived from the displacement-rate map (Figure S5). Seismicity between A^* and C^*, main- and foreshock hypocenters highlighted in orange. Mapped Cenozoic structures in gray and neotectonic structures in red. (b) Fault creep model and synthetic data. (c) Across-strike displacement profiles with data (black), nominal data uncertainty (gray), and model (pink). Displacement is accumulated in 202 days between events A^* and C^*. LOS: line-of-sight vector. See Figure 3d for along-strike view of the creep model and Figure S5 for uncertainty in map view.

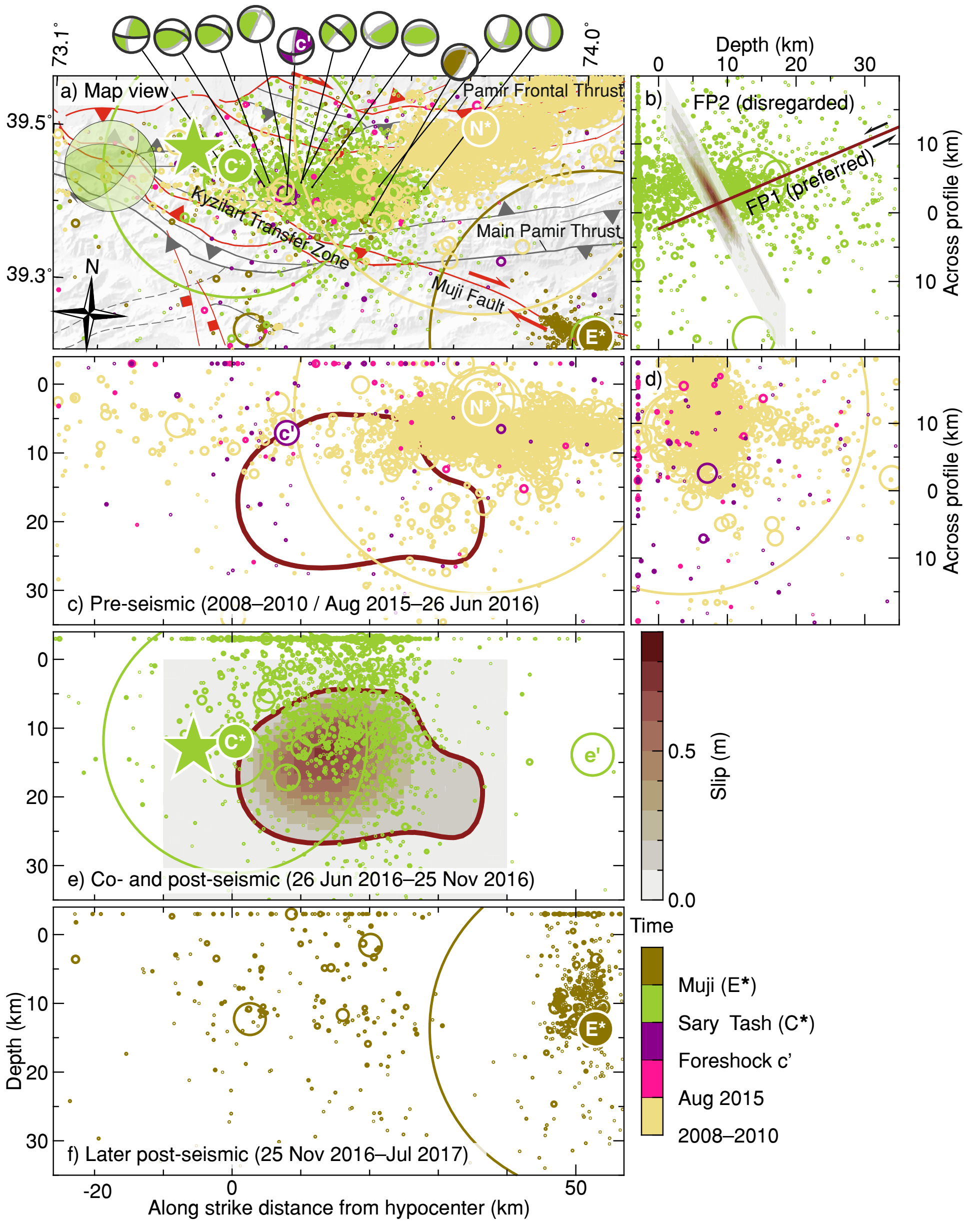

73.1°
74.0°
a) Map view
Pamir Frontal Thrust
N*
C*
c'
Kyzilart Transfer Zone
Main Pamir Thrust
Muji Fault
E*
39.5°
39.3°
N
Depth (km)
0
10
20
30
b)
FP2 (disregarded)
FP1 (preferred)
Across profile (km)
c) Pre-seismic (2008–2010 / Aug 2015–26 Jun 2016)
d)
e) Co- and post-seismic (26 Jun 2016–25 Nov 2016)
e'
Slip (m)
0.5
0.0
Time
Muji (E*)
Sary Tash (C*)
Foreshock c'
Aug 2015
2008–2010
f) Later post-seismic (25 Nov 2016–Jul 2017)
Depth (km)
-20
0
50
Along strike distance from hypocenter (km)

Figure 5. Time succession of seismicity and moment tensors of moderate earthquakes in the active part of the Main Pamir Thrust System; GEOFON focal mechanism (large beach ball); hypocenter location by NEIC (star); 2008–2010 seismicity from Schurr et al. (2014); hypocenter of the 2008 Nura earthquake (*N**; Sippl et al., 2014) and fore- and mainshocks discussed in the text (*c'*, *C**, *e'*, *E**). (a) Along-strike map view. Mapped Cenozoic structures in gray and neotectonic structures in red. (b, d) Across-strike profiles. (c, e, f) Along-strike profiles. (b) Aftershock seismicity and the two possible fault planes (He et al., 2018). FP1 is preferred, because aftershock seismicity concentrates in the hanging wall. (c, d) Seismicity before the Sary-Tash mainshock; 10% of maximum future slip contoured. (e) Early aftershock seismicity until subsequent Muji mainshock *E**. Co-seismic slip from He et al. (2018). (f) Later aftershock seismicity and spatial configuration with the Muji earthquake (*E**). Foreshock activity left out the future rupture area and grossly concentrated around the future hypocenter since *c'*. Aftershock seismicity concentrates in the hanging wall. Note the lesser depth extent of the Nura aftershock seismicity.

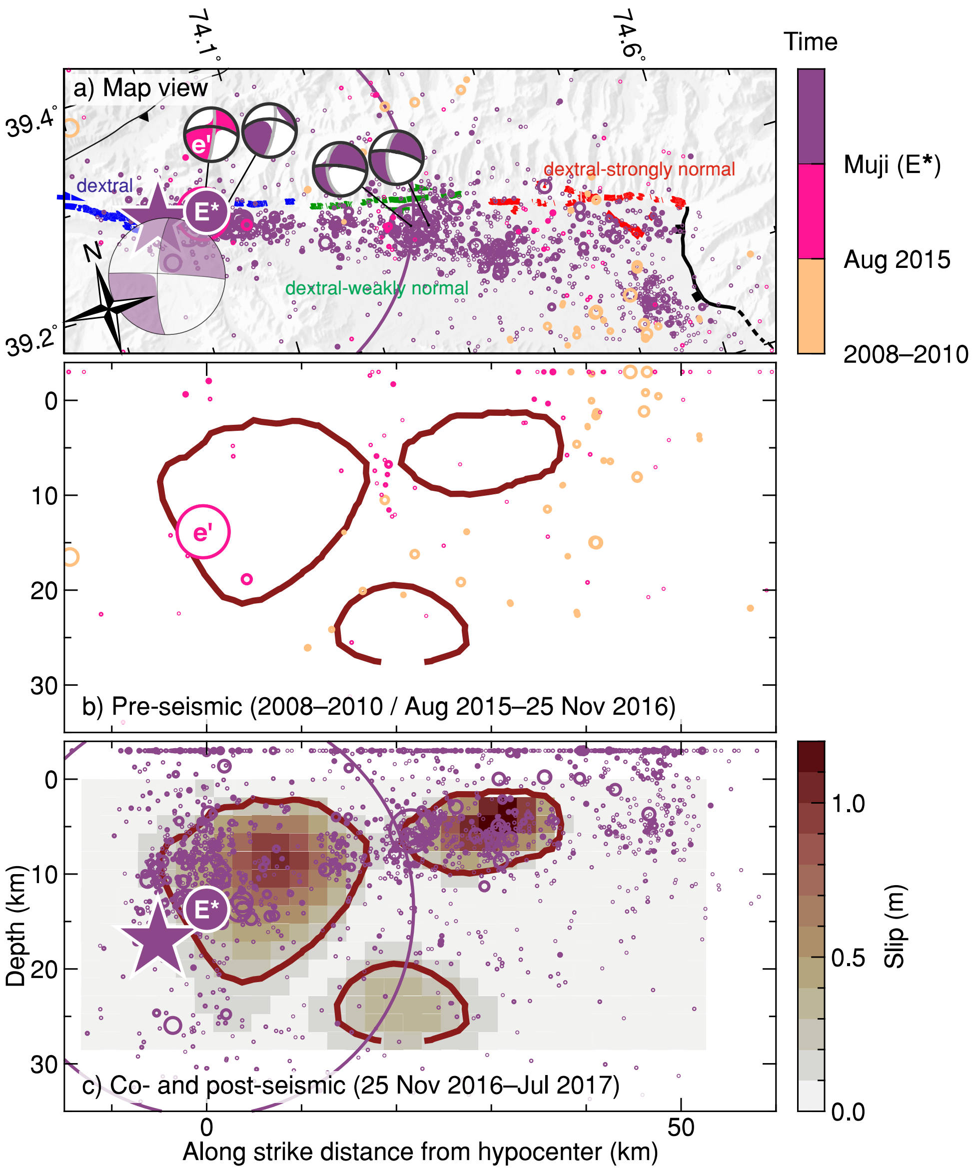

Figure 6. Time succession of seismicity and moment tensors of moderate earthquakes in the active part of the Muji Fault; GEOFON focal mechanism (large beach ball); hypocenter location by NEIC (star); 2008–2010 seismicity from Schurr et al. (2014); fore- and mainshock hypocenters (*e'*, *E**). (a) Along-strike map view. Surface traces (blue, green, red) of the Muji-Fault earthquake and other faults modified from T. Li et al. (2019) (b, c) Along-strike profiles. (b) Seismicity before the mainshock; 10% of maximum future slip contoured, the lowermost slip patch is not resolved. (c) Aftershock seismicity and co-seismic slip model (Bie et al., 2018). Foreshock activity left out the future rupture area. *e'* occurred 12 minutes before the mainshock, very close to the hypocenter location.

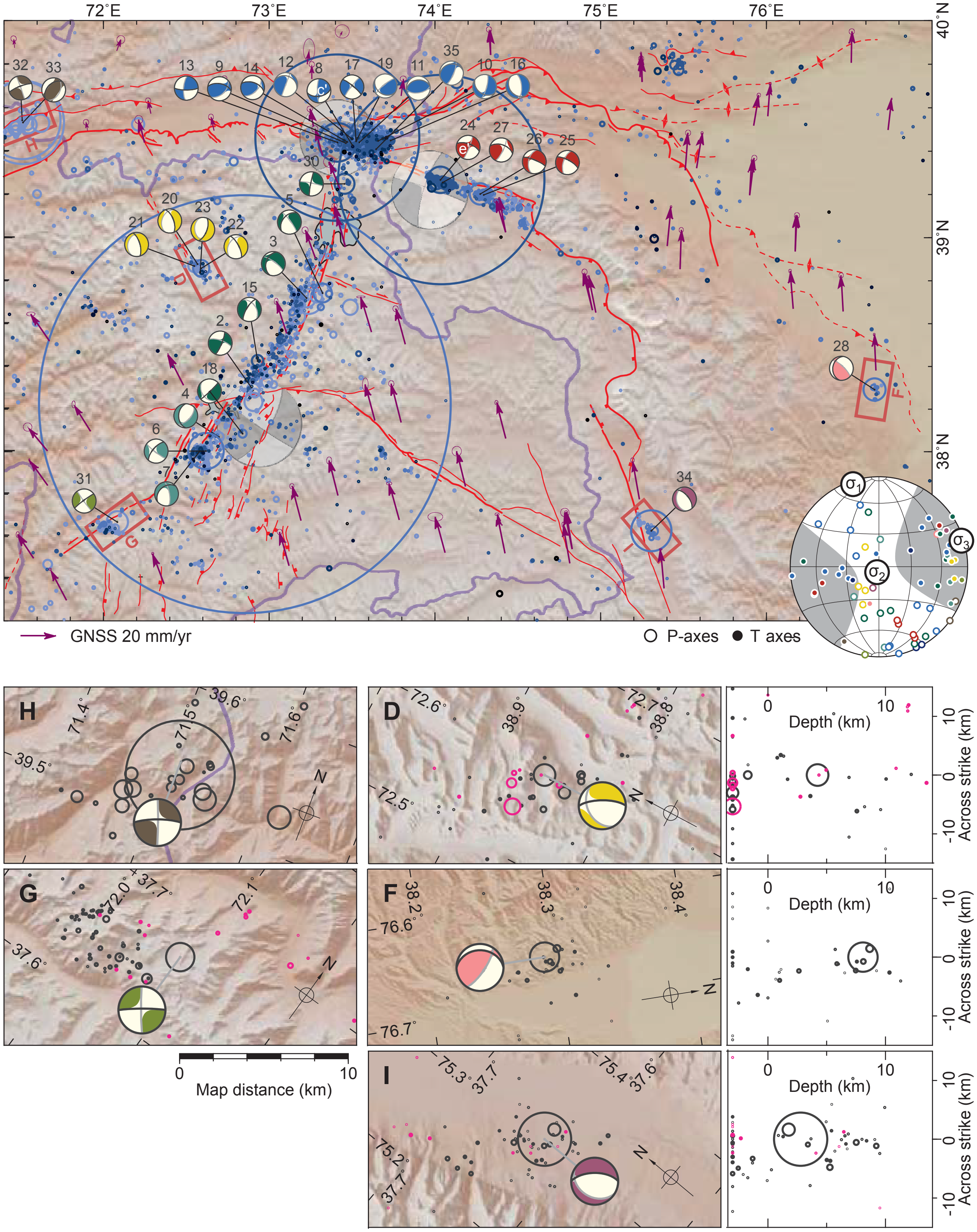
72°E
73°E
74°E
75°E
76°E
40°N
39°N
38°N
GNSS 20 mm/yr
P-axes
T axes
σ1
σ2
σ3
H
D
G
F
I
Depth (km)
Across strike (km)
Map distance (km)

Figure 7. Summary of moment tensor results. Moment tensors colored by earthquake sequence as in Figure 2 and numbered as in Table 1. Interpreted fault planes are marked in the beach balls in black; fault planes preferred by stress inversion are marked in the beach balls in dark gray; auxiliary plane in light gray. Top: regional overview map. GNSS vectors of Zubovich et al. (2010); Ischuk et al. (2013). Major neotectonic faults in red. Bottom: along-strike close-ups for sequences framed in the top subfigure; foreshocks (magenta); main- and aftershocks (black). (H, G) map views. (D, F, I) additional across-strike profiles . Inset: stereographic projection of moment- and stress tensor principal axes. Positive areas of the stress tensor are shaded. Lower hemisphere projection.

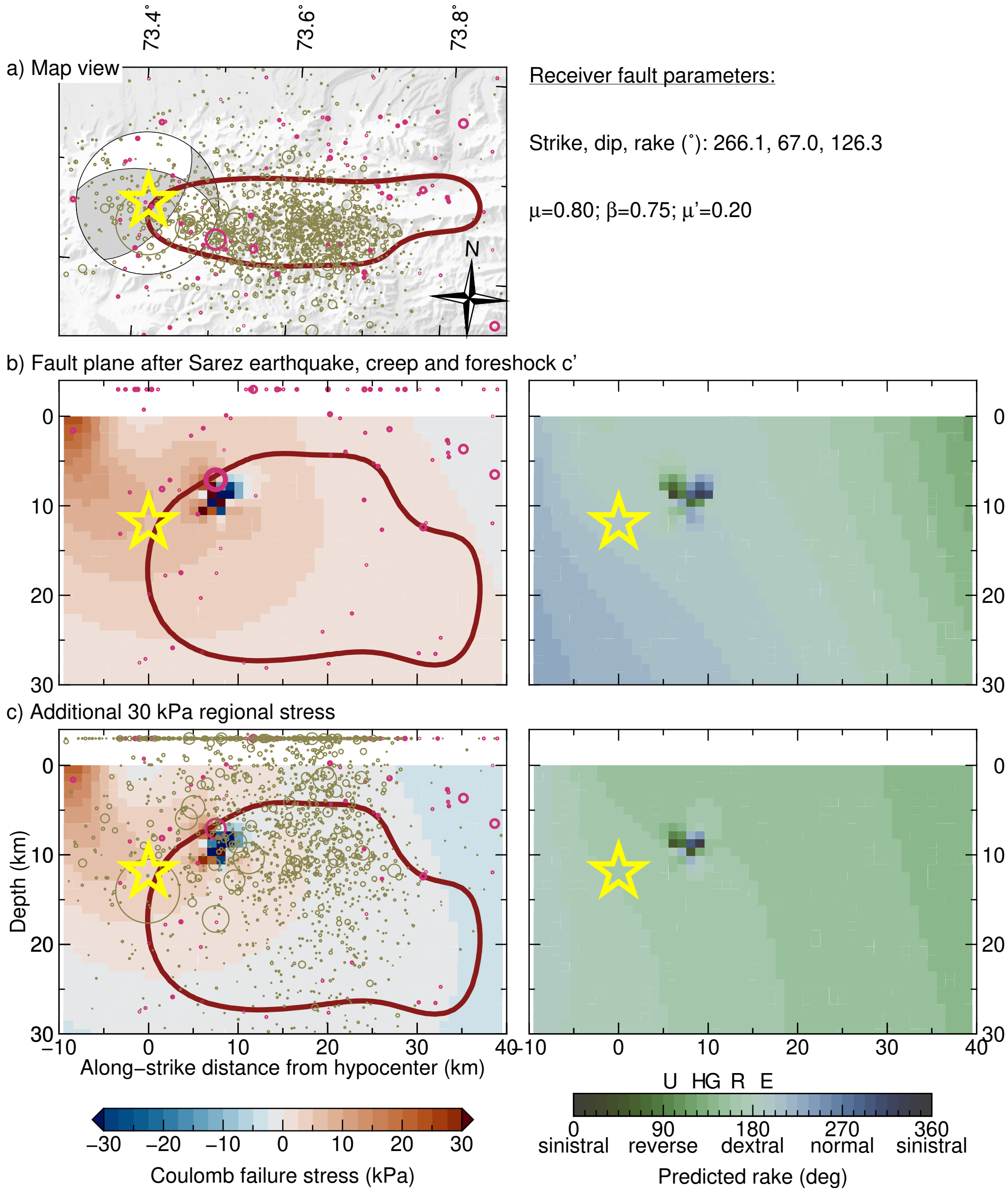

Figure 8. Coulomb failure stress changes on FP1 (Figure 5) with rupture extent (He et al., 2018) and hypocenter (star) of the Sary-Tash earthquake and seismicity before (magenta) and after the mainshock (khaki). (a) Map view. (b–c) Along-strike views onto the fault showing change in Coulomb failure stress (ΔCFS, left panels) and predicted rake (right panels) for the stress contributions denoted. Scale bar annotations: (N)EIC, (H)e et al. (2018), (G)EOFON, (R)egional stress (30 kPa), and (E)arthquake-induced (without regional stress). ΔCFS contributions and sensitivity analysis to β and μ in Figure S6.

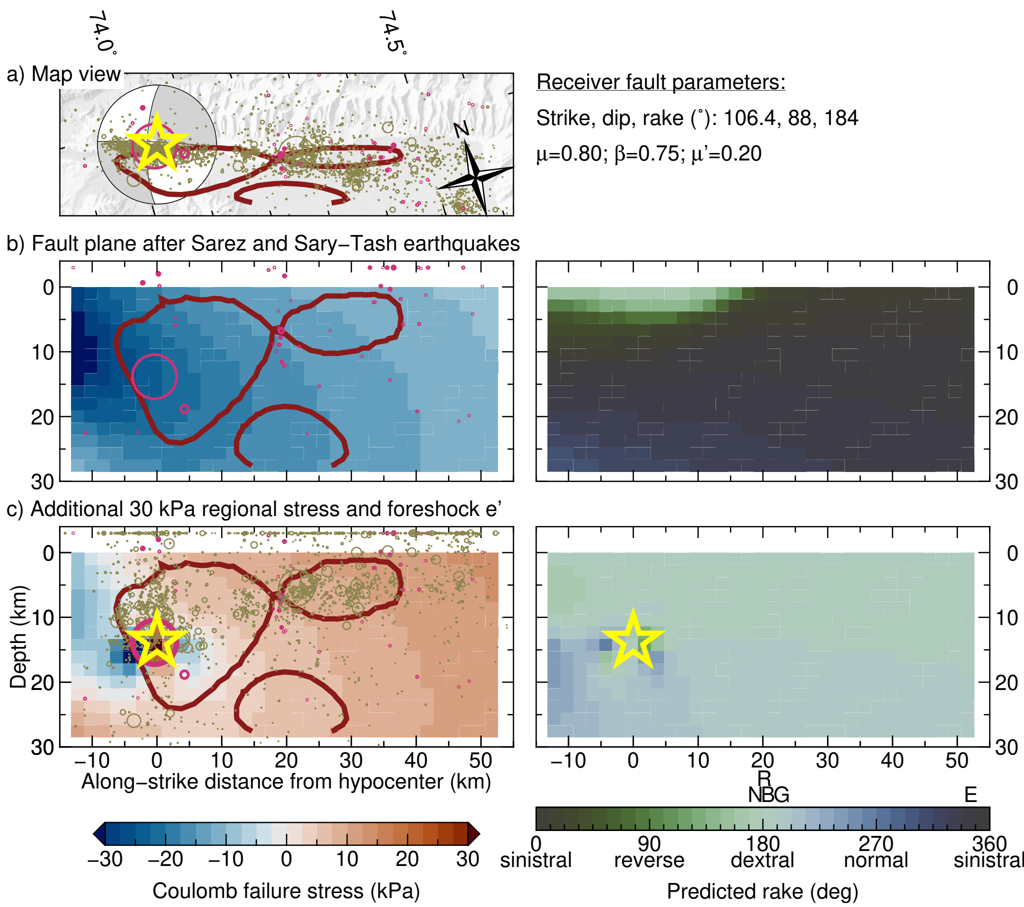

Figure 9. As Figure 8, but for the Muji fault. Scale bar annotations: (N)EIC, (B)ie et al. (2018), (G)EOFON, (R)egional stress, (E)arthquake-induced (without regional stress). ΔCFS contributions and sensitivity analysis to β and μ in Figure S8.